Ore Geology Reviews 132 (2021) 103993

Contents lists available at ScienceDirect

Ore Geology Reviews

journal homepage: www.elsevier.com/locate/oregeorev

Metallogenic mechanism of large manganese deposits from Permian manganese ore belt in western South China Block: New mineralogical and geochemical evidence

Hai Xu [a,b], Junbo Gao [a,b,*], Ruidong Yang [a,b], Kangning Feng [a,b], Longbo Wang [a,b], Jun Chen [c]

[a] College of Resources and Environmental Engineering, Guizhou University, Guiyang 550025, China
[b] Key Laboratory of Karst Georesources and Environment, Ministry of Education, Guizhou University, Guiyang 550025, China
[c] Institute of Geochemistry, Chinese Academy of Sciences, Guiyang 550081, China

ARTICLE INFO

Keywords:
Permian Mn deposit
Ore-forming mechanism
Mineralogy and geochemistry
Hydrothermal activity
South China Block

ABSTRACT

The Permian manganese (Mn) ore belt lies in western South China Block, and contains many large-medium Mn deposits. However, the genesis and metallogenic mechanism of these deposits remains a matter of debate. Here we shed light on this issue based on new mineralogical, geochemical, and Sr isotope data from the Changgou Mn deposit in the Zunyi orefield (Guizhou, SW China). The Mn orebodies occur as lenses and layers, and are hosted in carbonaceous-siliceous limestone, carbonaceous mudstone, and tuffaceous claystone. The ores show a variety of structures (e.g., detrital, brecciated, massive, and banded) and complex mineral compositions (e.g., galena, sphalerite, siegenite, molybdenite, barite, rutile, and monazite). The ore samples are characterized by chalcophile and siderophile element enrichments, low Al_2O_3/TiO_2 ratios (mean 10.36), high and varying Mn/Fe ratios (1.26–4.71), distinctly high REY (rare earth and yttrium) contents (mean 766.46 ppm), and high La/Ce (mean 1.04) and low Y/Ho (mean 28.17) ratios. The footwall and ore samples have $^{87}Sr/^{86}Sr$ ratios of 0.706897 to 0.707093. Integrated mineralogical and geochemical signatures indicate that the ore-forming fluids were most probably originated from hydrothermal activities related to early-stage Emeishan Large Igneous Province (ELIP) subaqueous volcanism. Redox proxies reveal that sedimentary conditions evolved from euxinic-anoxic (footwall deposition), through anoxic-suboxic (Mn mineralization), to oxic (hanging-wall deposition). Such changes were probably resulted from a coeval eustatic sea-level drop and enhanced seawater oxygen supply. Manganese was likely initially enriched in form of Mn^{2+}, and subsequently precipitated with oxidation, and then transformed into Mn carbonate during sediment diagenesis. To conclude, the tectono-hydrothermal activities and major environmental redox changes led by the ELIP volcanism have provided a favorable source-migration-sink system for the Mn mineralization.

1. Introduction

Manganese (Mn) ore deposits in China are geologically interesting not only because of their sizes (many reaching world-class), but also their widely varied metallogenic epochs from the Mesoproterozoic to the Early Mesozoic (Hou et al., 1997; Fan and Yang, 1999; Fu et al., 2014), although the majority of the ore deposits were formed in the Neoproterozoic, Devonian, Permian, and Carboniferous (Liu et al., 1989; Fan and Yang, 1999; Fu et al., 2014). In western South China Block, a Permian Mn ore belt lies in the intermediate to outer/marginal zone of the Emeishan Large Igneous Province (ELIP), and extends from Gexue (Yunnan Province) through Shuicheng-Nayong to Zunyi area (Guizhou Province) (Fig. 1a, b) (Liu et al., 1989, 2008; Hou et al., 1997). Studies over the past few decades have shown that the Zunyi Mn orefield, positioned in the core of ore belt and has many large-medium Mn deposits, possesses special metallogenic background and complex ore material compositions (Liu et al., 1989, 2008, 2015; Chen et al., 2003; Gao et al., 2018; Yang et al., 2018; Xu et al., 2020). More Mn deposits (e.g., Tongluojing, Shenxi, Yongan, and Xiaojingou, etc.) were successively discovered in recent years, showing that the Zunyi Mn orefield has great discovery potential.

As for the Mn metallogeny, some authors believed that the provenance of Mn was sourced from the weathering of Emeishan flood basalt (Liu et al., 1989; Chen et al., 2003). In recent years, many mineralogical

* Corresponding author at: College of Resources and Environmental Engineering, Guizhou University, Guiyang 550025, China.
E-mail address: gaojunbo1985@126.com (J. Gao).

https://doi.org/10.1016/j.oregeorev.2021.103993
Received 19 June 2020; Received in revised form 17 November 2020; Accepted 7 January 2021
Available online 14 January 2021

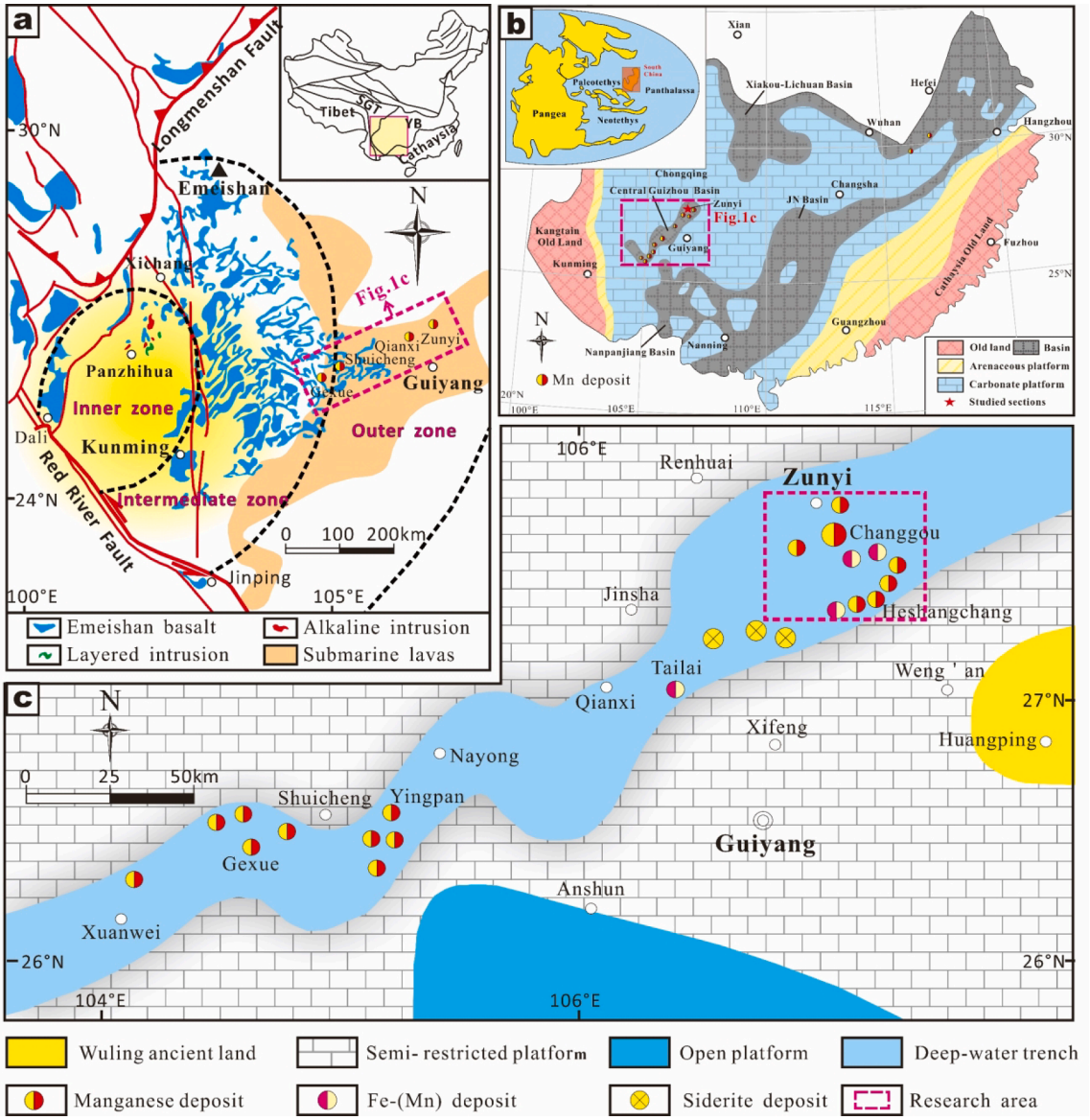

Fig. 1. (a). Distribution of the Emeishan Large Igneous Province (ELIP) in southwestern China (after Ukstins-Peate and Bryan, 2008); (b). Guadalupian paleogeography of South China (modified from Wei et al. (2016) and Chen et al. (2018)). (c). Lithofacies and paleogeography in central-western Guizhou during (end-Guadalupian) the Middle to Late Permian (after Chen et al. 2003).

and geochemical studies suggested that the Mn mineralization has a hydrothermal origin, but this view also being questioned since the Mn ore-forming scale were instead smaller close to the Emeishan LIP volcanism region (intense hydrothermal activity) (Fig. 1c; Liu et al., 2015; Gao et al., 2018; Yang et al., 2018; Xu et al., 2020). Recently, Wang et al. (2018) and Liu et al. (2019) proposed that these Mn deposits formation resembles the Nanhua (Cryogenian) Period sedimentary-type Mn deposits in south China, which was interpreted to have related to ancient natural gas seepage (Zhou et al., 2013), while this view is only inferred base on the rift origin of the Central Guizhou basin, and lacking detailed mineralogical and geochemical evidence.

To elucidate the actual ore-forming material source and mechanism, we studied the Changgou Mn deposit in the Zunyi orefield and presented new mineralogical, whole-rock geochemical, and Sr isotope data. We discussed the ore-forming material source, sedimentary environment evolution, metallogenesis, and ore-controlling factors of the end Permian Mn mineralization in western South China Block.

2. Geological setting

2.1. Regional geological setting

The Late Permian ELIP had a significant influence on the paleotectonics and paleogeography evolution of the western South China Block (Fig. 1; Ali et al., 2005; Zhou et al., 2006; Xu et al., 2013). The ELIP domal uplift caused the intensive activity of the regional deep faults, resulting in a short burst of extensive basaltic volcanism (258–260 Ma) (Ali et al., 2005; Zhou et al., 2006; Xu et al., 2013; Chen et al., 2018a). Lithostatic uplift caused by ELIP is considered to have been a major drive for basin development, through increasing in the extent of rifting and subsidence of the carbonate platform (He et al., 2006). In western South China Block, the differences subsidence of the restricted shallow-water carbonate platform (intermediate to outer zone of ELIP) has formed a NE-trending deep-water basin (the Central Guizhou basin), which extends from Gexue (Yunnan Province) to Shuicheng, Nayong, Qianxi, and Zunyi (Guizhou Province) (Fig. 1 c; Chen et al., 2003; He et al., 2006). Permian Mn mineralization in western South China Block was suggested

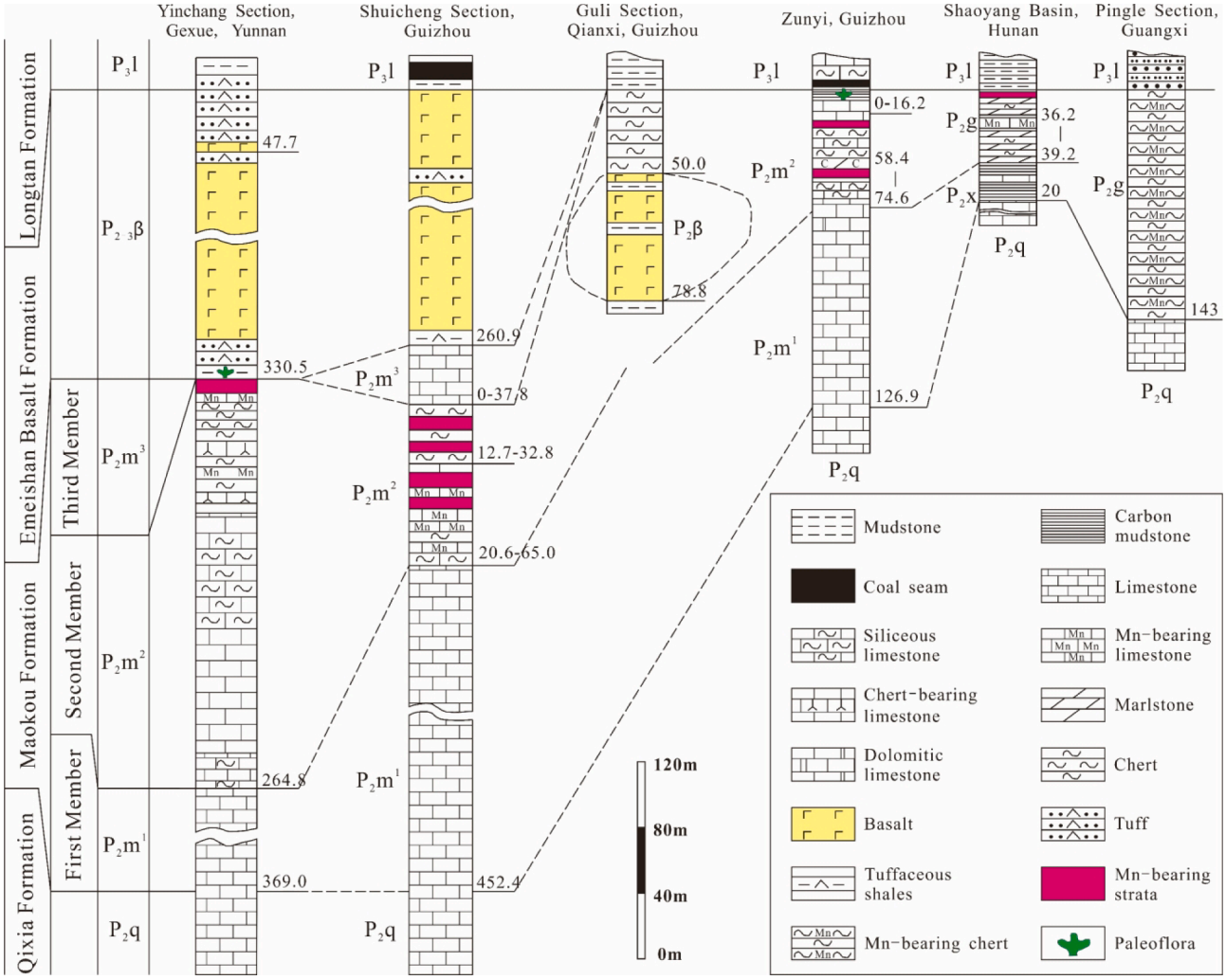

Fig. 2. Stratigraphic columns for the Permian Mn-bearing sequence in South China Block (modified after Liu et al., 2008; Gao et al., 2018).

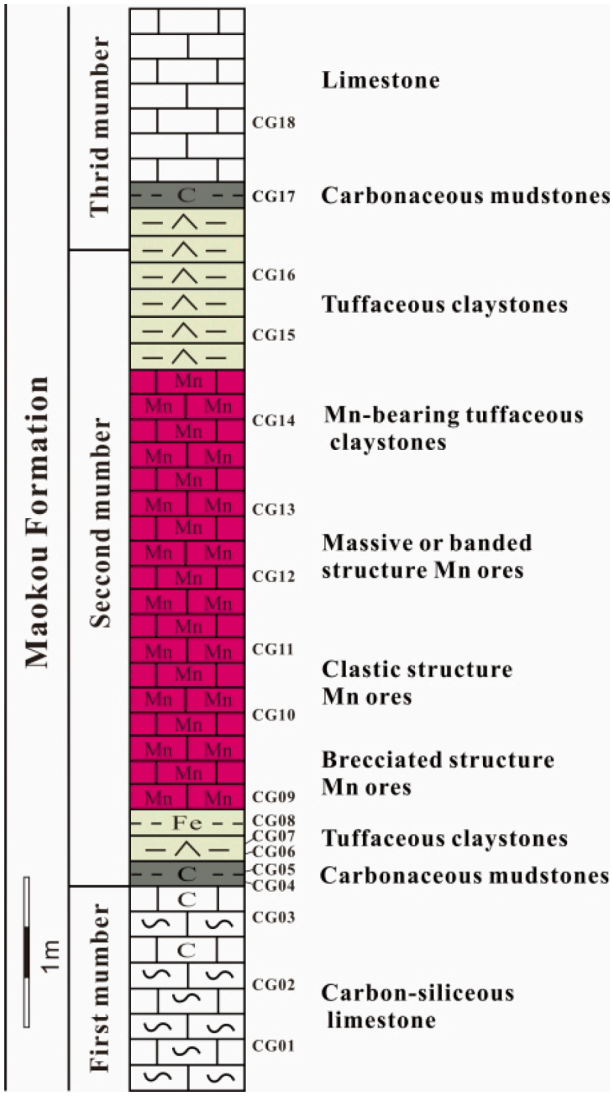

Fig. 3. Stratigraphic column for the Changgou Mn deposit in the Zunyi orefield (Guizhou, South China).

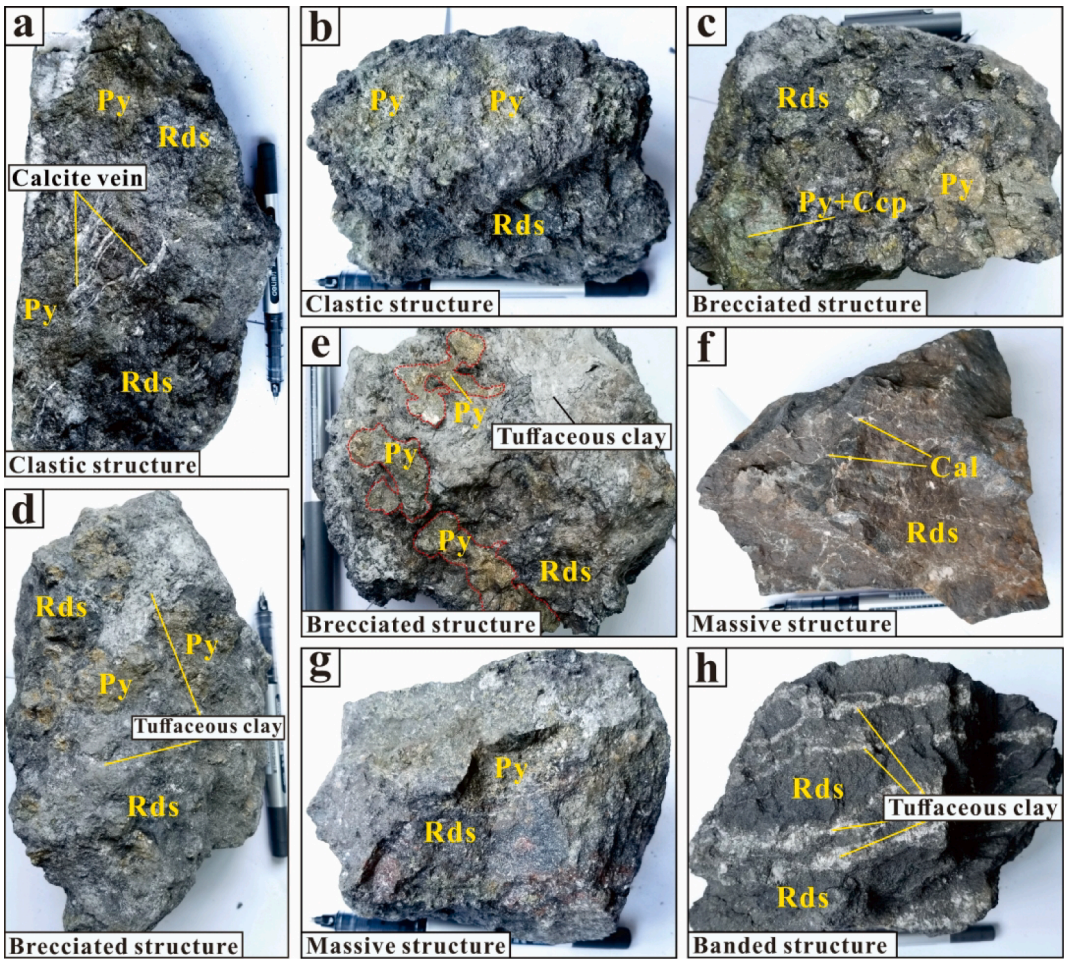

Fig. 4. Photographs of the Changgou ore hand-specimen in the Zunyi orefield (Guizhou, South China). (a) Detrital-textured Mn ores coexist with claystone and brecciated pyrite; (b) Detrital-textured Mn ores coexist with brecciated pyrite; (c) Brecciated ores coexist with brecciated chalcopyrite and pyrite; (d) Brecciated Mn ores coexist with claystone and brecciated pyrite; (e) Brecciated ore, with the detrital-textured ores filled by brecciated claystone and pyrite; (f) Massive Mn ore; (g) Massive Mn ores coexist with pyrite; (h) Banded ores (laminates are 0.1–3 cm), with interbedded tuffaceous claystone;

to have occurred in the early-stage of ELIP activity (262.5 Ma) (Yan et al., 2020), and coeval with the rapid rifting of the Central Guizhou basin (Fig. 1c; Liu et al., 1989; Chen et al., 2003; Yang et al., 2018).

2.2. Ore deposit geology

The Permian Mn ore belt extends across eastern Yunnan to western Guizhou in SW China (Fig. 1c). Over than 10 large-medium Mn deposits were discovered in the Central Guizhou basin (350 km long and 25–50 km wide) (Fig. 1c), which major ones including the Tongluojing, Changgou, Shenxi, Yongan, Shaba, Shiliugou, Changzheng, Nancha, and Tongziwo (Zunyi orefield), the Tailai (Qianxi orefield), the Yingpan (Nayong orefield), the Xujiazhai (Shuicheng orefield), and the Gexue (Xuanwei orefield) (Fig. 1c; Liu et al., 1989). These Mn deposits were hosted by the Permian Maokou Formation (Fm.) carbonaceous-siliceous limestone, carbonaceous mudstone, and tuffaceous claystone (Fig. 2). The locally-called "Bainitang layer" (a siliceous layer) is commonly developed at the bottom of the Mn ore layer. The hanging-wall consists of the third member of the Maokou Fm., Longtan (Xuanwei) Fm., or Emeishan flood basalt (Fig. 2; Liu et al., 1989; Chen et al., 2003).

The Changgou Mn orefield (106°57′22″E, 27°38′47″N) is located to the northeastern of the Central Guizhou basin. Ore bodies occur as lenses and layers and are hosted in the Moukou Fm. (Figs. 2-3). The orebody distribution is clearly controlled by the Central Guizhou basin (Liu et al., 2015). The orebodies are 2 to 7.5 m thick and thin toward the deposit margin. The footwall comprises green tuffaceous claystone and black carbonaceous mudstone (0.1–0.5 m thick), and including numerous detrital pyrite (Fig. 3). The tuffaceous claystone layer was considered closely related to early-stage Emeishan pillow basalt and mafic volcaniclastics formation (Yan et al., 2020). The "Bainitangceng" siliceous layer and carbonaceous-siliceous limestone of varying thickness are developed around and below the tuffaceous claystone layer and Mn orebodies. The hanging-wall comprises grey tuffaceous claystone and black mudstone (max 2–3 m thick). The black mudstone is overlain by tens of meters of thick bioclastic-limestone.

3. Samples and methods

A total of seventeen samples were collected from the bottom to top across a profile (CG01 to CG18) at Changgou (106°57′22″E, 27°38′47″N) (Fig. 3), which include three footwall carbonaceous-siliceous limestone (CG01 ~ 03), four carbonaceous mudstone and tuffaceous claystone (CG04 ~ 07), six Mn ore-bearing carbonate (CG09 ~ 14), and three hanging-wall tuffaceous claystone and one limestone (CG15 ~ 18).

Mineral contents of the samples were observed by optical light microscopy and Electron Probe Microanalysis (EPMA; including back-scattered electron (BSE) imaging) at the Guizhou University and the

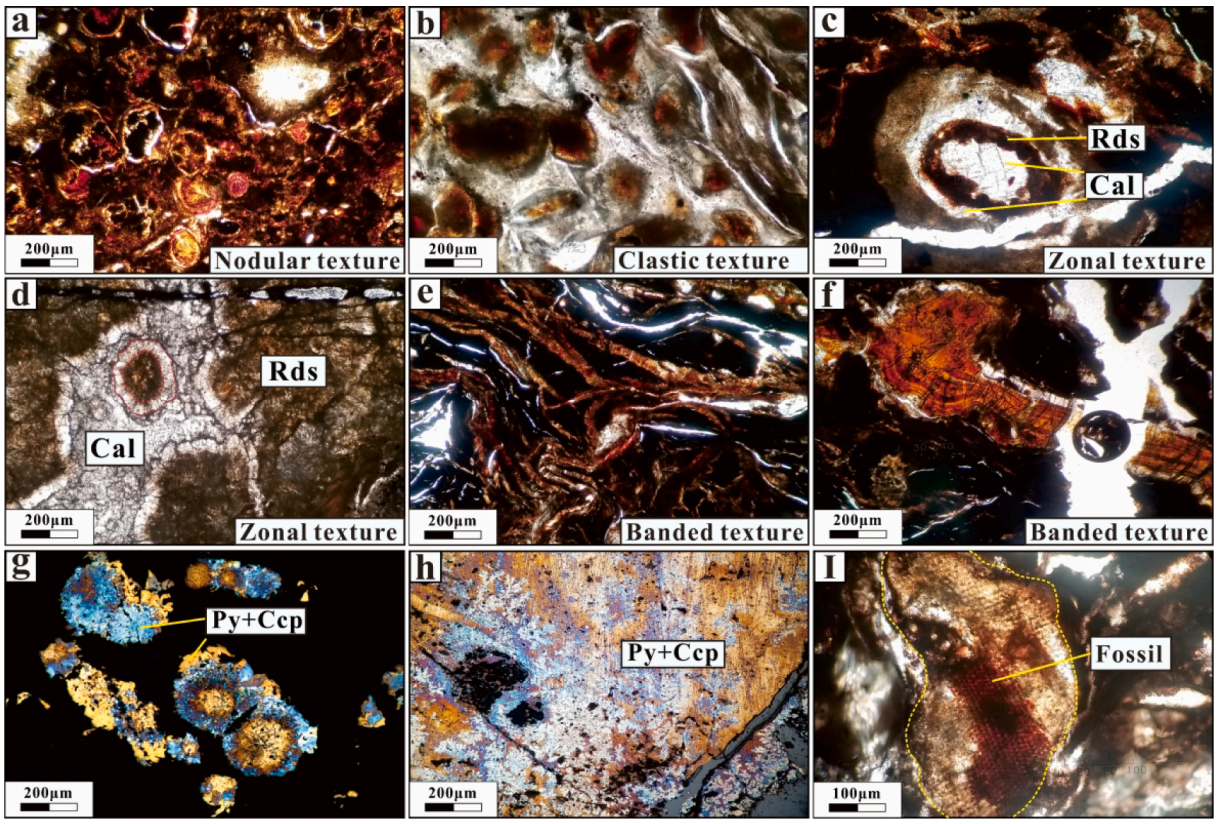

Fig. 5. Microphotographs (crossed polar /reflected light) of the Changgou Mn ores. (a) Concentrically-zoned nodules display sharply banding and coexisting rhodochrosite, capillitite, and manganoan calcite cement (reflected light); (b) Detrital texture composed mainly of rhodochrosite and cemented by zoned capillitite (reflected light); (c) Annular texture shows banded colloform layers, coexisting with calcite, rhodochrosite, manganoan calcite, and capillitite cement from inside out (reflected light); (d) Annular texture exhibit banded colloform layers, coexisting rhodochrosite and manganoan calcite cement from inside to outside (reflected light); (e) Banded texture (reflected light); (f) Banded rhodochrosite displaying a rhythmic structure growth (reflected light); (g) Annular pyrite coexist with chalcopyrite (transmitted light); (h) Chalcopyrite filled by banded pyrite (transmitted light); (i) Acanthosis fossil mineralized into rhodochrosite (reflected light).

Xi'an Center of Geological Survey, Geology Survey, respectively. The EPMA conditions were using a 15 kV accelerating voltage, 1.00×10^{-8} A beam current, and 1 μm beam diameter.

The major elements were measured on all samples at the ALS Minerals (Guangzhou) by inductively coupled plasma atomic emission spectrometry (ICP-AES). Each sample (0.5 g) was mixed with $Li_2B_4O_7$ and $LiBO_2$, and then placed in a sealed bomb and heated in the furnace (1000 °C). Afterward, add the dilute HNO_3 and HCl in the sample until completely dissolved. Finally, the resultant liquid was analyzed by ICP-AES. The trace elements were measured on all samples at the State Key Laboratory of Ore Deposit Geochemistry, Institute of Geochemistry, Chinese Academy of Science by inductively coupled plasma mass spectrometer (ICP-MS) with a PerkinElmer ELAN DRC-e quadrupole (Q-ICP-MS). Each sample (50 mg) was completely digested by a mixed HF and HNO_3 solution, using the Rh (40 ng/mL^{-1}) as the internal standard. The analytical accuracy was better than 5%.

Whole-rock Strontium isotope analyses were made at the State Key Laboratory of Geological Processes and Mineral Resources (GPMR), China University of Geosciences (Wuhan) by Triton Plus thermal ionization mass spectrometer (TIMS), following the procedures of Li et al. (2016). Isotopic ratios corrected for mass fractionation were normalized to an $^{86}Sr/^{88}Sr$ ratio of 0.119400. Measurements of the Sr standard NBS987 yielded an $^{87}Sr/^{86}Sr$ ratio of 0.710300 ± 4 (2σ).

4. Results

4.1. Ore structural and textural features

Field observations reveal the coexistence of various ore structures such as detrital (Fig. 4a, b), brecciated (Fig. 4c–e), massive (Fig. 4f, g), and banded (Fig. 4h). In hand specimen, the brecciated and detrital structures are composed mainly of brecciated/detrital Mn carbonates, brecciated pyrite (Fig. 4a–e), chalcopyrite (Fig. 4c), claystone, and calcite veins (Fig. 4a). Similar detrital and brecciated structures were also documented in the Gexue Mn orefield, but rarely found in the Shuicheng-Nayong Mn orefield (Liu et al., 2008). Massive and banded Mn ores generally exist in the middle to lower parts of orebodies, and massive ores consist mainly of massive Mn carbonates with minor calcite veins (Fig. 4f, g). Banded Mn ores consist mainly of Mn carbonates with interbedded banded tuffaceous claystone (Fig. 4h).

Under the microscope, the ore samples have a variety of textures including nodular (Fig. 5a), detrital (Fig. 5b), annular (Fig. 5c, d), and banded (Fig. 5e, f). The nodular texture is composed mainly of many Mn carbonate nodules that display concentric growth and thin to moderately-thick layering (Fig. 5a). In contrast, the detrital texture is composed mainly of rhodochrosite, which is cemented by zonal capillitite (Fig. 5b). Notably, the annular texture exhibits concentric rhythmic cementation, coexisting as calcite, rhodochrosite, manganoan calcite, or capillitite from inside out (Fig. 5c, d). In some cases, many cores seem to have coalesced into a single-large crystal during the growth (Fig. 5d). The banded Mn ore comprises a rhythmic growth rim

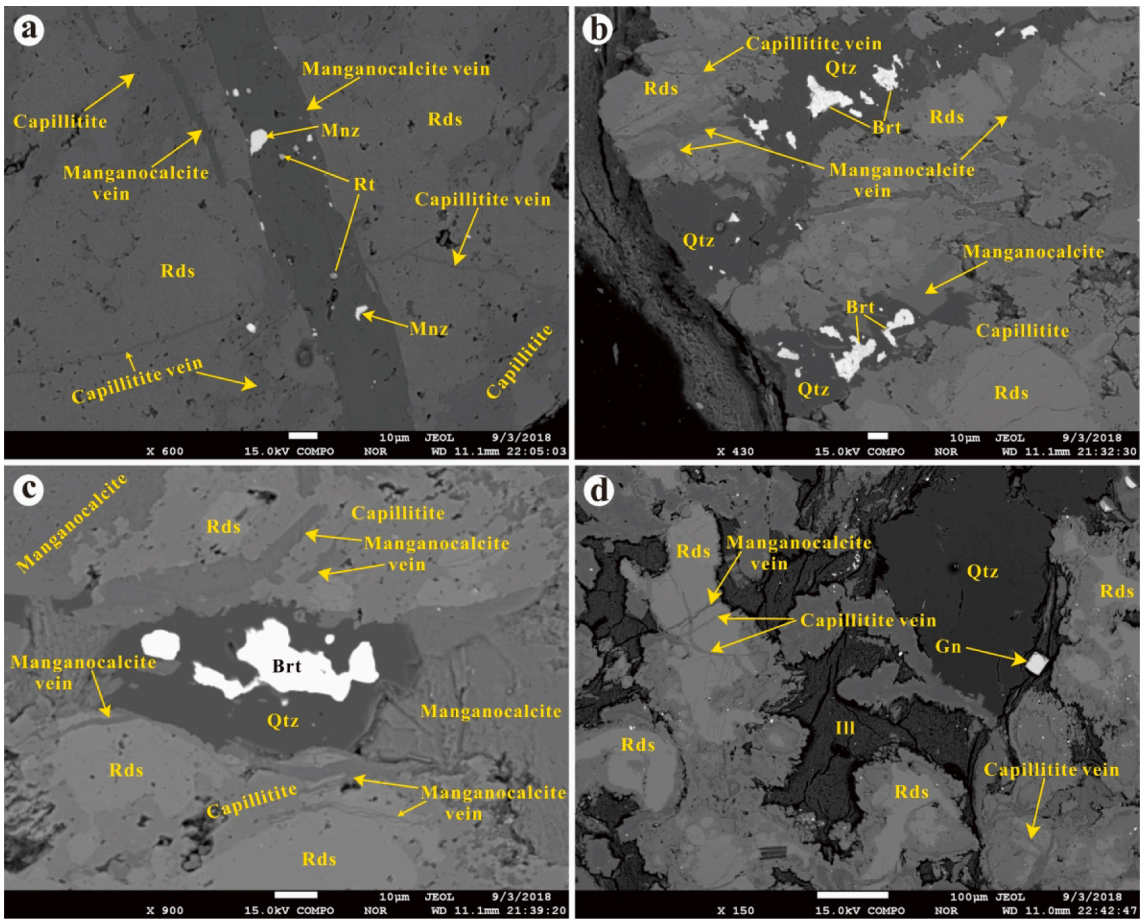

Fig. 6. BSE images of the Changgou Mn ore samples (Guizhou Province, SW China). (a) Manganoan calcite vein crosscuts rhodochrosite and capillitite; (b) Capillitite vein crosscuts rhodochrosite; (c) Manganoan calcite and capillitite vein crosscuts rhodochrosite; (d) Manganoan calcite vein crosscuts rhodochrosite and capillitite vein.

(Fig. 5f), and similar to that of the concentrically laminated ore nodules. In many samples, rhodochrosite or manganoan calcite is the initial cementing material of individual micronodules, and these cemented micronodules then underwent later diagenetic cementation (Fig. 5a–f). Moreover, sulfides minerals (e.g. pyrite and chalcopyrite) were observed in the ore samples (Fig. 5g, h). In some cases, pyrite coexists with chalcopyrite to form an annular texture (Fig. 5g). Rhodochrosite is reddish-brown due to its Fe content, and chalcopyrite has steady covellite due to oxidation. Acanthosis fossils (replaced by rhodochrosite) were also observed in some ore samples (Fig. 5i), reflecting isomorphic substitution of Ca^{2+} and Mg^{2+} in the carbonates by Mn^{2+}, forming diagenetic Mn-Ca-Mg carbonates (Nyame et al., 2002).

4.2. Mineralogy

The EPMA results are shown in Supplementary Table 1 and illustrated in Figs. 6 and 7. Ore minerals include mainly rhodochrosite, capillitite, and manganoan calcite (Fig. 6a–d), whilst the gangue minerals include mainly illite, quartz, pyrite, monazite, barite, rutile, galena, sphalerite and zircon, and minor molybdenite, xenotime, and siegenite (Fig. 7a–l). Three different mineralization stages were recognized based on EPMA results, and crosscutting relations and mineral associations. Stage I rhodochrosite mineralization (Fig. 6a) is crosscut by stage II capillitite and stage III manganoan calcite veins (Fig. 6 and 7), and coexists with pyrite, sphalerite, monazite, molybdenite, and siegenite. Stage II capillitite mineralization is crosscut by stage III manganoan calcite veins (Fig. 6a) and coexists with monazite and sphalerite. While stage III manganoan calcite mineralization as veins cross-cut rhodochrosite and capillitite (Fig. 6a–d), and coexists with monazite and rutile (Fig. 6a).

Clay minerals (esp. illite) are the main minerals at Changgou Mn deposit, except in Mn-bearing minerals (Fig. 7). In addition, granular sphalerite grains are present on the margins and inside rhodochrosite and illite (Fig. 7a), and cubic galena grains are included in the clastic-quartz (Fig. 7b). Meanwhile, irregularly-shaped barite inclusions are found in quartz (Fig. 7c), and rutile occurs as detrital-shape within rhodochrosite and illite (Fig. 7d), implying the high-temperature phases were possibly resulted from thermo-tectonic events (Liakopoulos et al. 2001). Notably, monazite generally occurs as individual detrital-shape crystals and distributed within rhodochrosite (Fig. 7e). Monazite also occurs as veins crosscutting pyrite and rhodochrosite (Fig. 7f, g). Under BSE imaging, zircon, xenotime, and pyrite are generally granularly distributed on the margin or included in illite, manganoan calcite, and quartz (Fig. 7h–j). Also, fine-grained molybdenite and massive siegenite were found in rhodochrosite (Fig. 7k, l). The mineral assemblage from Changgou is comparable to that of typical hydrothermal deposits at Vani (Greece) (Liakopoulos et al., 2001; Papavassiliou et al., 2017), Novo Natal (SW Amazonia, Brazil) (Albuquerque et al., 2017), and Bahia Concepcion Bay (Mexico) (Rodríguez-Díaz et al., 2018).

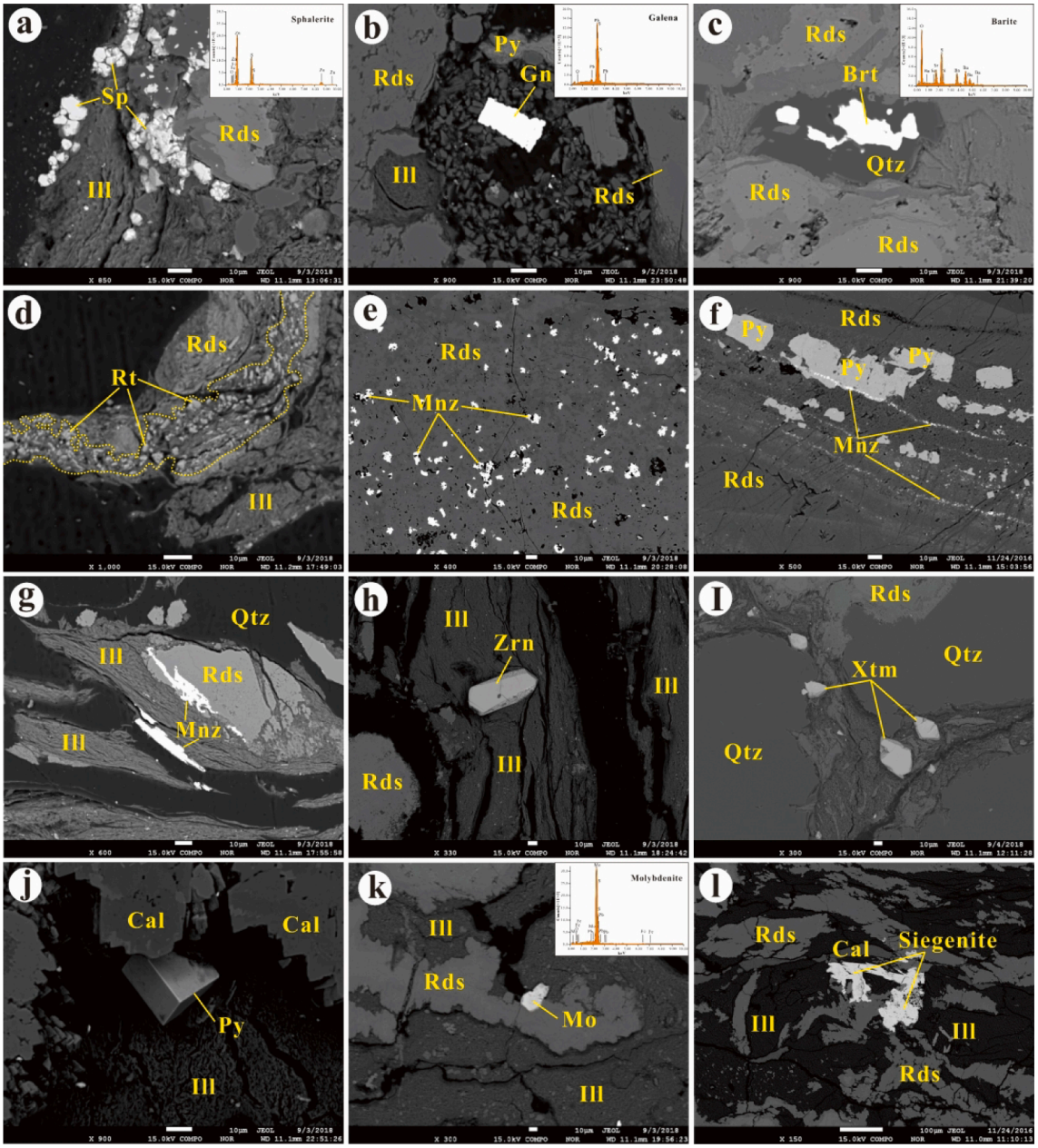

Fig. 7. BSE and EDS images of the Changgou Mn ore samples. (a) Granular sphalerite on the margin of rhodochrosite, quartz and illite; (b) Euhedral galena in clastic quartz; (c) Granular barite in quartz; (d) Fine-grained rutile in rhodochrosite; (e) Fine-grained monazite in rhodochrosite; (f) Disseminated/veined monazite crosscuts pyrite and rhodochrosite; (g) Monazite veinlets crosscuts rhodochrosite; (h) Euhedral zircon in illite; (i) Xenotime on the margin of quartz and illite; (j) Euhedral pyrite in illite; (k) Fine-grained molybdenite on the margin of rhodochrosite and illite; (l) Irregular-shaped siegenite on the margin of rhodochrosite and illite.

Table 1
Major element compositions (wt.%) of the Changgou Mn deposit.

Sample	Rock (ore) type	Al_2O_3	CaO	TFe_2O_3	K_2O	MgO	MnO	Na_2O	P_2O_5	SiO_2	SO_3	SrO	TiO_2	V_2O_5	LOI
CG-01	Siliceous limestone	1.01	28.80	0.64	0.15	0.53	0.24	/	0.08	38.48	1.39	0.18	0.01	0.04	27.74
CG-02	Siliceous limestone	0.48	41.00	0.35	0.07	0.48	0.63	/	0.02	22.03	0.72	0.32	/	/	33.87
CG-03	Siliceous limestone	1.32	23.10	0.78	0.23	0.63	0.90	/	0.24	47.93	1.43	0.15	0.02	/	22.69
CG-04	Carbon clay	7.26	1.45	5.30	1.45	0.62	0.02	/	0.17	47.93	1.52	/	0.28	0.10	34.94
CG-05	Carbon clay	7.86	0.11	5.85	1.57	0.67	0.02	0.01	0.02	46.9	0.86	/	0.29	0.16	35.48
CG-06	Claystone	23.29	0.44	5.42	3.99	1.86	0.03	0.19	0.14	53.38	9.85	0.04	0.76	0.08	9.08
CG-07	Claystone	11.64	0.42	35.77	1.67	0.89	0.14	0.28	0.05	24.18	>34	0.06	0.52	0.17	23.74
CG-09	Mn ore	4.31	7.59	8.66	0.51	2.56	38.71	0.07	0.07	9.83	13.85	0.04	0.25	0.04	27.98
CG-10	Mn ore	11.12	5.94	12.26	1.17	3.19	23.65	0.22	0.04	17.51	5.98	0.07	0.81	0.08	24.67
CG-11	Mn ore	14.48	3.17	12.27	1.51	2.45	19.79	0.22	0.05	22.69	11.95	0.05	1.99	0.03	21.54
CG-12	Mn ore	5.45	8.43	19.64	0.51	2.57	23.54	0.13	0.04	12.61	25.50	0.11	0.48	0.02	24.81
CG-13	Mn ore	10.56	2.71	12.84	1.14	2.85	26.23	0.14	0.02	18.95	2.74	0.03	2.40	0.03	24.21
CG-14	Mn ore	8.89	2.81	17.30	0.87	3.55	24.27	0.10	0.02	16.75	3.32	0.03	1.09	<0.01	25.23
CG-15	Claystone	25.19	1.32	10.02	2.74	2.13	0.43	0.28	0.02	40.56	12.45	0.05	4.39	<0.01	11.32
CG-16	Claystone	28.52	0.74	3.25	3.28	1.65	0.05	0.35	0.01	46.28	3.15	0.04	5.54	<0.01	9.18
CG-17	Carbon mudstone	21.43	2.58	6.55	2.62	1.95	1.11	0.19	0.22	46.58	9.99	0.05	1.90	0.06	13.09
CG-18	Siliceous limestone	8.00	9.78	6.73	0.54	2.92	3.75	1.89	0.04	45.26	6.73	0.04	1.02	0.01	16.68

4.3. Geochemistry

4.3.1. Major element compositions

Major element compositions of the Changgou samples are shown in Table 1. The Changgou ore samples have varying concentrations of TFe_2O_3 (8.86–19.64 wt%), MnO (19.79–38.71 wt%), SiO_2 (9.83–22.69 wt%), Al_2O_3 (4.31–14.48 wt%), CaO (2.71–8.43 wt%), and TiO_2 (0.25–2.40 wt%), with minor MgO (2.45–3.55 wt%), Na_2O (0.07–0.22 wt%), K_2O (0.51–1.17 wt%), and P_2O_5 (0.02–0.07 wt%). In addition, the footwall and hanging-wall samples have highly varying content of TFe_2O_3 (0.35–35.77 wt%), SiO_2 (22.03–53.38 wt%), Al_2O_3 (0.48–28.52 wt%), CaO (0.11–28.8 wt%), and TiO_2 (0.01–5.54 wt%), but low content of MnO (0.02–3.75 wt%). Our results show that Changgou Mn deposit has relatively high Fe content (mean 13.82 wt%) and depletion in P (mean 0.04 wt%). In addition, the ore samples have Al_2O_3/TiO_2 values of 4.40 to 17.24 (mean 10.36), but low Fe/Mn values of 1.33 to 4.94 (mean 2.33).

4.3.2. Trace element compositions

The trace element compositions of the Changgou samples are listed in Table 2. The lower wallrocks (tuffaceous claystone) are characterized by Cr, V, Co, Ni, Pb, Cu, Sb, Zn, Mo, and U enrichments relative to the average Post-Archean Australian Shale (PAAS) (Taylor and McLennan, 1985), whilst the Mn ore samples are characterized by Cr, V, Co, Ni, Pb, Cu, Sb, Zn, Ba, Sr, Mo, and U enrichments. Conversely, the hanging-wall are significantly enriched in Li, Nb, Ta, Zr, Hf, Ga, and slightly enriched in Cr, V, Ni, Sb, Cu, and U (Table 2; Fig. 8). Overall, the lower wall-rock (tuffaceous claystone) and ore samples are characterized by the chalcophile and siderophile element enrichments. However, in additional to slightly enrichments in the chalcophile and siderophile elements, the hanging-wall is also distinctly enriched in lithophile elements (e.g., Li, Nb, Ta, Zr, Hf) (Fig. 8).

REE compositions of the Changgou samples are listed in Table 2. The lower wallrock (tuffaceous claystone) samples show slightly elevated total (Σ) REE contents of 433.35 to 1308.04 ppm (mean 674.32 ppm), distinct light rare earth elements (LREE) enrichments, and negative Ce (Ce/Ce^*= 0.33–0.65) and Eu (Eu/Eu^*= 0.49–0.59) anomalies. All the Mn ore samples have very high ΣREE (239.01 to 1136.78 ppm, mean 766.46 ppm), distinct LREE enrichments (LREE/HREE = 6.09), and negative Ce (Ce/Ce^* = 0.37–0.87) and Eu (Eu/Eu^* = 0.55–0.74) anomalies. In contrast, the hanging-wall samples have relatively low ΣREE (205.56–529.72 ppm, mean 305.59 ppm), moderate LREE enrichments, and slightly positive Ce (Ce/Ce^*= 1.21–1.51) anomalies and slightly positive Eu (Eu/Eu^*= 1.02–1.49) anomalies. In addition, the Y/Ho and La/Ce ratios of the ore samples are of 22.59–50.55 (mean 28.20) and 0.58–1.27 (mean 1.04), respectively.

4.3.3. Sr isotope compositions

Strontium isotope compositions of the Changgou samples are listed in Table 3. The $^{87}Sr/^{86}Sr$ ratios of all sample range from 0.706897 to 0.707093 (mean 0.706971), therein the $^{87}Sr/^{86}Sr$ ratios of foot wallrock (siliceous limestone) samples range from 0.706897 to 0.706912 (mean 0.706905, n = 2), and the $^{87}Sr/^{86}Sr$ ratios of Mn carbonate ore samples range from 0.706929 to 0.707093 (mean 0.706994, n = 6). This shows an increasing $^{87}Sr/^{86}Sr$ trend from the footwall to the orebody.

5. Discussion

5.1. Genesis of Changgou Mn deposit

As mentioned by previous studies that the element ratios and concentrations can be used to determine the genesis of Mn deposits (Toth, 1980; Condie, 1993; Nath et al., 1997; Hein et al., 2008). In general, the Al_2O_3/TiO_2 ratios of mafic volcanic rocks vary from 3.00 to 14.00 (Condie, 1993; Sugitani et al., 1996; Hayashi et al., 1997), whilst those of Phanerozoic pelagic sedimentary rocks are of 20 to 30 (Sugitani et al., 1996). The Changgou ore samples have Al_2O_3/TiO_2 ratios (4.4–17.24, mean 10.36) comparable to mafic volcanic rocks. Moreover, high or low Mn/Fe ratios ($0.1 < Mn/Fe < 10$) generally produced in those of sedimentary exhalative (SEDEX)-type Mn deposits, since the characteristically fractionated of Fe and Mn, whereas this ratio is closer to 1 in those of hydrogenous deposits (Nicholson et al., 1997). In our case, the Mn/Fe ratios of the Changgou ore samples (1.33–4.94, mean 2.33) are thus comparable to those of sedimentary exhalative deposits.

Certain trace elements (e.g., V, As, Zn, Ba, Sb, Cu, Pb, Li, Sr, and Mo) tend to be enriched in hydrothermal Mn deposits (Nicholson, 1992; Sasmaz et al., 2014). All the studied ore samples are enriched in Cr, V, Co, Ni, Pb, Cu, Sb, Zn, Ba, Sr, Mo, and U, similar to hydrothermal Mn ores from the Elazığ (Turkey) (Sasmaz et al., 2014), Cheshmeh-Frezi (Iran) (Maghfouri et al., 2017), and Vani (Greece) (Papavassiliou et al., 2017). In addition, the Cu (26.00–56.80 ppm; mean 41.9 ppm), Pb (12.80–62.90 ppm; mean 37.81 ppm), and Zn (27.40–78.90 ppm; mean 46.83 ppm) concentrations in the ore samples are high, and the presence of chalcopyrite, galena, and sphalerite (Fig. 7a, b) in the ore samples typically reflects the primarily contribution of hydrothermal fluids (Nicholson, 1992; Hein et al., 2008; Sasmaz et al., 2014). The presence of barite (Fig. 7c) in the ore samples are likely responsible for the Ba and Sr enrichments. Meanwhile, the Co and Ni enrichments are likely associated with the Co–(Ni) sulfides (i.e., siegenite, Fig. 7l) in the ore samples, which also reflects hydrothermal mineralization (Hein et al.,

Table 2
Trace and rare element compositions (ppm) of the Changgou Mn deposit.

Sample	CG-1	CG-2	CG-3	CG-4	CG-5	CG-6	CG-7	CG-9	CG-10	CG-11	CG-12	CG-13	CG-14	CG-15	CG-16	CG-17	CG-18
Li	5.50	3.37	6.43	28.50	25.10	29.30	23.50	10.80	25.40	62.50	18.70	16.80	17.10	87.40	90.80	27.00	22.40
V	343.00	30.20	110.00	606.00	897.00	568.00	862.00	351.00	575.00	446.00	218.00	457.00	175.00	521.00	576.00	568.00	213.00
Cr	189.00	36.40	129.00	724.00	830.00	1334.00	562.00	160.00	188.00	118.00	50.30	232.00	25.70	206.00	199.00	346.00	110.00
Co	2.65	1.60	2.96	9.41	29.30	32.80	144.00	67.70	195.00	180.00	72.60	15.80	89.80	30.60	9.68	47.90	16.00
Ni	58.60	25.60	46.20	217.00	484.00	75.20	346.00	117.00	400.00	388.00	156.00	56.60	259.00	116.00	45.50	138.00	53.70
Cu	15.10	4.74	11.20	40.30	60.30	42.20	77.90	38.80	36.60	62.10	26.00	31.20	56.80	91.70	76.60	48.00	24.60
Zn	64.00	20.40	34.60	138.00	102.00	100.00	79.90	42.30	39.60	37.90	78.90	27.40	54.90	38.90	36.10	47.60	56.00
Ga	1.31	0.74	1.88	9.30	9.88	28.40	14.50	11.80	23.70	28.10	15.40	23.20	19.90	47.00	50.60	48.70	16.70
Ge	0.47	0.32	0.59	2.68	3.05	3.15	10.40	4.14	5.48	6.00	7.69	4.97	6.65	4.12	2.16	3.58	3.28
As	5.58	2.90	5.48	25.70	36.80	35.20	100.00	72.00	94.50	35.40	66.50	13.00	30.10	45.90	20.40	135.00	41.10
Rb	6.27	3.16	8.55	53.60	57.40	105.00	37.70	12.80	20.90	27.10	9.74	23.80	16.90	42.30	51.60	51.70	13.00
Sr	2156.00	3175.00	1758.00	216.00	122.00	603.00	544.00	483.00	821.00	555.00	1049.00	404.00	420.00	510.00	490.00	698.00	564.00
Zr	17.30	8.23	22.10	134.00	157.00	435.00	216.00	99.90	265.00	520.00	148.00	637.00	217.00	1275.00	1588.00	1409.00	566.00
Nb	1.36	0.72	2.29	11.20	12.50	43.60	24.80	11.90	39.00	56.60	15.30	72.70	23.50	141.00	175.00	141.00	66.10
Mo	16.60	3.35	5.94	38.50	59.40	31.00	138.00	19.60	4.90	4.35	10.80	1.52	1.24	3.06	1.26	2.31	2.19
Cd	5.18	0.24	0.54	2.20	1.20	4.30	4.13	1.96	1.53	2.27	5.04	0.56	2.92	0.88	0.61	3.50	2.18
Sb	2.27	0.78	1.54	9.74	17.70	7.57	27.00	19.10	24.90	7.63	6.29	1.47	4.87	3.60	1.58	5.09	3.05
Ba	27.80	19.10	42.20	173.00	520.00	412.00	453.00	67.40	180.00	197.00	143.00	135.00	103.00	339.00	417.00	321.00	120.00
Hf	0.41	0.20	0.53	3.24	3.54	10.30	5.66	2.51	7.76	11.40	3.70	13.90	5.73	28.10	33.90	34.30	12.20
Ta	0.12	0.07	0.15	0.77	0.78	2.49	1.39	0.68	2.60	3.41	0.92	4.56	1.57	8.98	10.50	7.72	3.86
W	0.28	0.22	0.33	0.95	1.01	2.43	1.63	1.08	2.72	3.29	1.14	3.36	2.84	4.14	4.57	1.52	1.21
Tl	0.82	0.06	0.19	1.97	2.03	1.53	11.10	0.54	0.18	0.22	0.09	0.20	0.11	0.74	0.60	0.74	0.71
Pb	5.12	2.20	5.39	34.90	64.30	41.10	46.80	42.10	62.90	70.00	13.30	12.80	25.80	40.10	17.60	57.30	30.60
Th	1.21	0.59	1.53	5.17	8.55	22.20	13.10	4.31	20.60	14.50	5.64	14.40	7.98	21.30	23.70	34.40	13.60
U	9.38	3.42	6.26	50.30	69.90	38.50	26.10	3.60	7.80	13.40	9.28	7.91	7.40	19.90	24.80	32.70	24.90
La	16.30	12.60	19.70	134.00	159.00	525.00	133.00	116.00	254.00	240.00	218.00	39.80	132.00	37.90	28.40	71.80	36.00
Ce	9.61	6.43	13.50	80.90	89.80	296.00	136.00	91.00	264.00	229.00	176.00	68.50	118.00	91.30	74.00	228.00	88.10
Pr	2.57	1.87	3.24	18.30	21.70	48.20	11.90	14.00	54.50	60.90	61.20	8.44	33.20	8.22	7.18	18.20	7.80
Nd	10.50	7.49	13.40	70.70	83.20	136.00	44.50	57.20	209.00	231.00	252.00	31.50	119.00	28.60	26.80	67.60	28.50
Sm	1.88	1.29	2.50	10.50	13.80	15.70	7.39	9.38	39.80	43.60	51.30	7.17	24.10	6.85	8.07	14.40	4.94
Eu	0.36	0.25	0.48	1.96	2.37	2.64	1.41	2.24	7.28	7.25	8.79	1.81	4.34	2.61	3.36	5.30	2.29
Gd	1.93	1.25	2.62	9.46	13.20	16.90	8.55	12.50	34.70	33.40	43.50	7.62	19.50	8.91	10.40	15.60	4.26
Tb	0.27	0.19	0.37	1.42	1.96	3.10	1.24	1.80	5.96	5.44	7.07	1.52	3.36	1.70	1.81	2.43	0.66
Dy	1.65	1.09	2.25	8.76	11.20	21.50	8.08	11.60	36.10	31.80	40.30	10.20	20.30	10.60	10.60	13.40	3.82
Ho	0.35	0.23	0.47	1.95	2.23	4.94	1.88	2.71	7.24	6.33	7.58	2.02	4.01	2.02	1.98	2.51	0.78
Er	0.96	0.61	1.26	5.52	5.99	14.10	5.45	7.36	20.00	17.70	19.70	5.23	10.80	5.15	5.13	6.44	2.17
Tm	0.13	0.08	0.16	0.76	0.80	1.96	0.76	0.92	2.88	2.63	2.71	0.73	1.51	0.74	0.74	0.88	0.32
Yb	0.79	0.48	1.00	4.87	5.04	12.20	4.86	5.26	18.70	17.30	17.10	4.63	9.72	4.90	4.99	5.67	2.12
Lu	0.12	0.07	0.15	0.74	0.74	1.80	0.74	0.80	2.62	2.42	2.36	0.64	1.36	0.70	0.71	0.79	0.31
Y	16.20	10.30	20.30	83.50	88.10	208.00	100.00	137.00	180.00	146.00	179.00	49.20	90.60	46.00	46.70	76.70	23.50
REE	47.41	33.92	61.11	349.85	411.03	1100.04	365.76	332.77	956.78	928.77	907.61	189.81	501.20	210.20	184.17	453.02	182.06
REE + Y	63.61	44.22	81.41	433.35	499.13	1308.04	465.76	469.77	1136.78	1074.77	1086.61	239.01	591.80	256.20	230.87	529.72	205.56
LREE/HREE	6.66	7.51	6.38	9.45	8.99	13.38	10.59	6.75	6.46	6.94	5.47	4.82	6.10	5.05	4.07	8.49	11.62
Ce/Ce*	0.33	0.29	0.38	0.35	0.33	0.36	0.65	0.47	0.52	0.45	0.37	0.87	0.43	1.21	1.24	1.51	1.23
Eu/Eu*	0.58	0.60	0.57	0.59	0.53	0.49	0.54	0.63	0.59	0.56	0.55	0.74	0.59	1.02	1.12	1.07	1.49
La/Ce	0.57	0.48	0.66	0.59	0.62	0.72	1.20	0.74	0.90	0.81	0.66	1.17	0.72	1.19	1.10	1.40	0.83
Y/Ho	46.15	45.37	42.92	42.82	39.51	42.11	53.19	50.55	24.86	23.06	23.61	24.36	22.59	22.77	23.59	30.56	30.21
Ce_{anom}	−0.50	−0.56	−0.44	−0.47	−0.50	−0.47	−0.21	−0.35	−0.29	−0.35	−0.44	−0.07	−0.38	0.07	0.08	0.17	0.08

Abbreviations: $Ce/Ce^*=2 \times Ce_N/(La_N + Pr_N)$, $Ce_{anom} = lg[3Ce_{SN}/(2 \times La_{SN} + Nd_{SN})]$, where N indicates that ratios were normalized to chondrite (Sun and McDonough 1989), SN = PAAS-normalized Shale (McLennan, 1989).

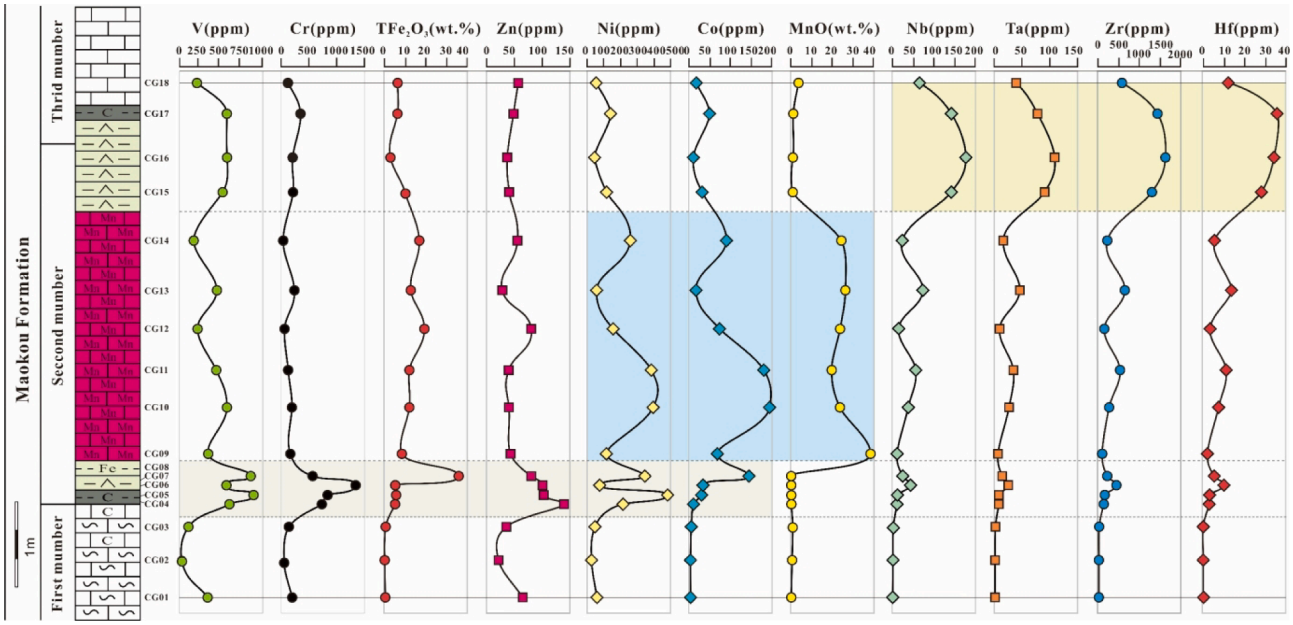

Fig. 8. Lithological and trace element geochemical stratigraphy for the Permian Changgou Mn deposit.

Table 3
Strontium isotope compositions of the Changgou Mn deposit.

Sample no.	Description	$^{87}Sr/^{86}Sr$	Error(2σ)	Date source
CG01	Siliceous limestone	0.706897	0.000009	This study
CG03	Siliceous limestone	0.706912	0.00001	
CG09	Mn carbonate	0.706929	0.000006	
CG10	Mn carbonate	0.706964	0.000008	
CG11	Mn carbonate	0.706971	0.000009	
CG12	Mn carbonate	0.707004	0.000006	
CG13	Mn carbonate	0.707001	0.000007	
CG14	Mn carbonate	0.707093	0.000005	
Permian seawater	–	0.707000	–	Veizer and Compston (1974), Korte et al. (2003), Veizer et al. (1999)
Late PermianMaokou stageseawater in the South China Block	Carbonate	0.707073-0.707568	–	Tian and Zeng (1995), Qu et al. (2018)
Basalts from the outer zone of ELIP	–	0.7048-0.7669	–	Fan et al. (2008), Lai et al. (2012), Bagherpour et al. (2018)
Crust	–	0.7119	–	Palmer and Elderfield (1985)
Mantle	–	0.7035	–	Palmer and Edmond (1989)

2008). The high Mo contents probably reflect high-temperature hydrothermal leaching > 310 °C from felsic to mafic volcanism (Hein et al., 2008). The Changgou ore samples have slightly Mo enrichment (1.24–19.6 ppm, mean 7.07 ppm), probably reflecting low-temperature hydrothermal conditions (Sasmaz et al., 2014).

The Co/Zn ratios in hydrothermal Mn deposits are of 0.15, whereas those typical of hydrogenous Mn deposits are higher than 2.5 (Toth, 1980). The Changgou ore samples have Co/Zn (0.58–4.92, mean 2.4) ratios similar to those of hydrothermal Mn deposits. In the ternary Ni-Co-Zn, Fe-Mn-(Ni + Cu + Co)*10, and Co/Zn vs. Co + Ni + Cu diagrams (Bonatti et al., 1972; Toth, 1980; Choi and Hariya, 1992; Nicholson, 1992), most of the ore samples plotted within or around the hydrothermal field (Fig. 9a–c). This is probably due to metal-rich (e.g., Co-rich fluids) hydrothermal fluids input, which enhanced the Co/Zn ratios and shifts some ore samples toward the Co end-member in the discrimination diagrams. In the 5*(Cu + Ni)-100*(Zr + Y + Ce)-(Fe + Mn)/4 discrimination diagram (Fig. 9d; Josso et al., (2017), most of the Changgou Mn ore samples are classified to have had a mixed hydrothermal-hydrogenous origin. A more likely explanation is that the REY-rich hydrothermal input (see below) and resulting in relatively high REY contents of ore samples resemble hydrogenous origin (Josso et al., 2017). Notably, considering to the ELIP also developed the Co-Mn, Cu, Te, REE, etc. mineralization related to the hydrothermal activity of basaltic magma (Xu et al., 2013; Shellnutt, 2014), probably caused the Mn mineralization together with Co-REE enrichments.

Hydrothermal deposits have lower ΣREY (ΣREE + Y) than those of hydrogenous deposits, and they show clear LREE enrichments (Hein et al., 1990; Sabatino et al., 2011). In addition, hydrothermal Mn ores present a wide range of ΣREY (Mills et al., 2001). In our case, the ΣREY contents of the ore samples are wide-range (239.01–1136.78 ppm, mean 766.46 ppm) and slightly higher than that of hydrothermal ores (Table 4; Hein and Kosk, 1987; Nath et al., 1997; Del RioSalas et al., 2008; Sasmaz et al., 2014), but lower than hydrogenous Mn ores (Table 4; Glasby et al., 1997; Wiltshire et al., 1999; Zhong et al., 2017) and modern oceanic Fe-Mn nodules or crusts (Chen et al., 2018b; Zhong et al., 2019). In particular, the Changgou ore samples have chondrite-

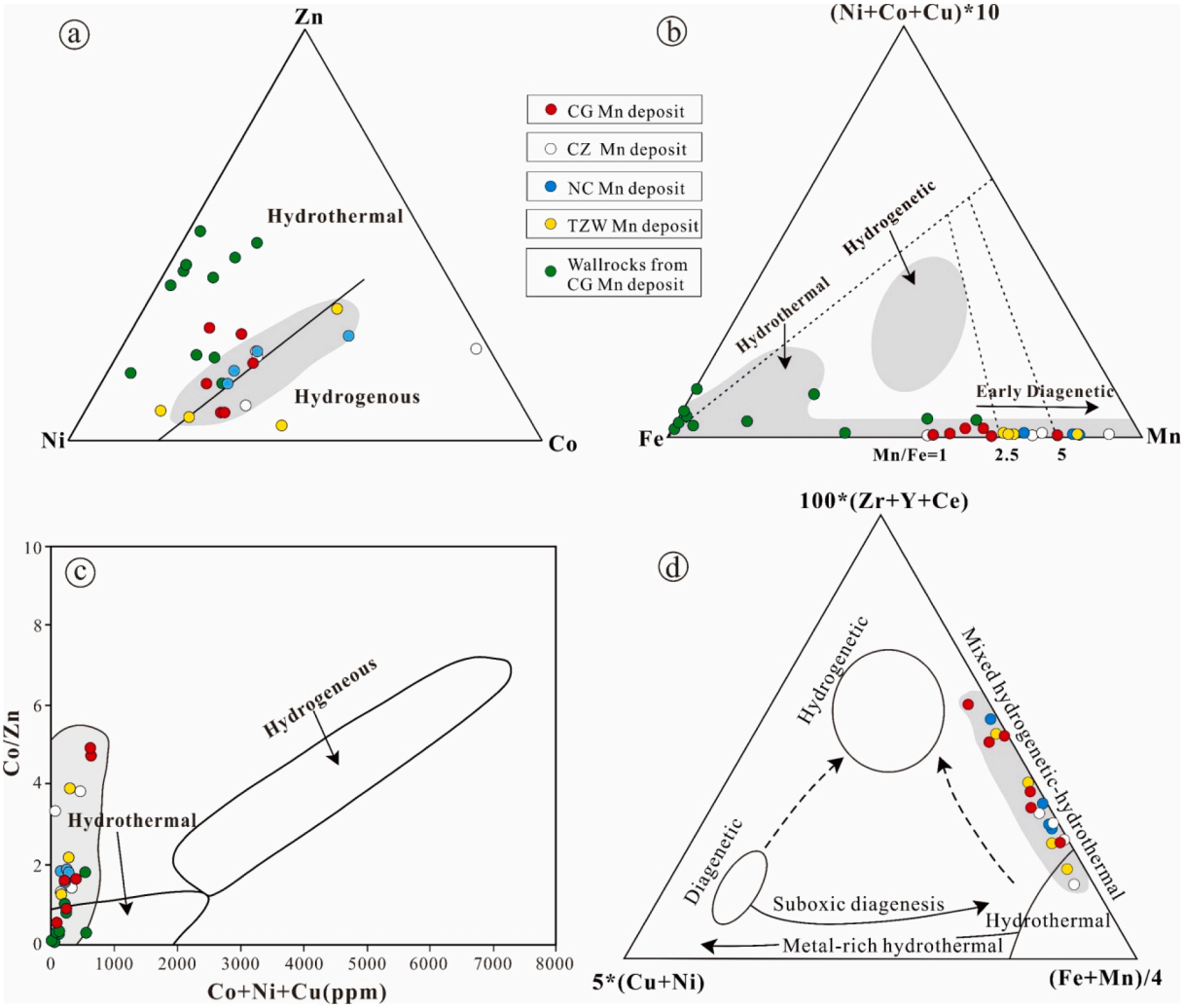

Fig. 9. Hydrothermal vs. hydrogenous Mn deposit discrimination diagrams for the Zunyi deposits: (a) Ternary Co-Ni-Zn (Choi and Hariya, 1992; Nicholson, 1992); (b) Ternary Mn-Fe-10*(Ni + Cu + Co) (base map after Bonatti et al., 1972; Toth, 1980); (c) Co/Zn vs. Co + Ni + Cu (Toth, 1980); (d) 5*(Cu + Ni)-(Fe + Mn)/4–100*(Zr + Y + Ce) (after Josso et al., 2017). Mn deposit name abbreviations: CG: Changgou; CZ: Changzheng; NC: Nancha; TZW: Tongziwo.

normalized LREE enrichments (LREE/HREE = 4.82–6.94), and strongly-negative Ce and slightly-negative Eu anomalies (Table 2; Fig. 10c). These signatures are very similar to the lower wallrock (tuffaceous claystone) (Fig. 10b) implies that the Mn mineralization was probably originated from volcanism or associated hydrothermal activity. Meanwhile, the REE fractionation features of the Changgou ores also resemble that of hydrothermal Mn ores from the Elazığ (Turkey) (mean ΣREE = 677.60 ppm) (Sasmaz et al., 2014), Rodriguez Triple Junction (Indian Ocean) (mean ΣREE = 647.90 ppm) (Nath et al., 1997), and Santa Rosalía (México) (mean ΣREE = 563.10 ppm) (Del RioSalas et al., 2008) (Table 4). Thus, despite ΣREY contents of the Changgou ores are high (Tables 2 and 4), but fall within the range of hydrothermal Mn ores (Hein et al., 1987; Sasmaz et al., 2014). In addition, the disseminated/veined REY-rich monazite crosscutting pyrite and rhodochrosite (Fig. 7f-g) also supported that the REY enrichments in the Mn ores were sourced from REY-rich hydrothermal fluids.

The La/Ce ratios of hydrothermal Fe-Mn ores are similar to seawater (~2.8), while those of hydrogenous Fe-Mn ores are distinctly lower (~0.25; Nath et al. 1997). The Changgou ore samples have La/Ce ratios of 0.58 to 1.27 (mean 1.04), reflecting the significant influence of hydrothermal activity for ore formation. In addition, the Y/Ho ratios of seawater generally range from 44 to 74, whereas those of chondrites, volcanic rocks, and shales are of 26–28 (Nozaki et al., 1997; Bau and Dulski, 1999; Liakopoulos et al., 2001). The Changgou ore samples have Y/Ho ratios (22.59–50.55, mean 28.17) clearly lower than those of seawater, but close to those of chondrites, volcanic rocks, and shales. Meanwhile, considering the influence of coeval volcanism or associated hydrothermal activities in/around the Changgou area (Liu et al., 1989, 2008), probably resulted in lower Y/Ho ratios of the ore samples. Hence, integrating the other indicators (e.g., Mn/Fe, Al_2O_3/TiO_2, and Co/Zn ratios, REE features), the lower Y/Ho ratios in the Mn ores samples have resulted primarily from hydrothermal activity.

Previous studies suggested that the Permian seawater has $^{87}Sr/^{86}Sr$ ratios of 0.7070 to 0.7078 (Veizer and Compston, 1974; Veizer et al., 1999; Korte et al., 2003), whilst the Late Permian (end-Guadalupian) seawater (South China Block) has $^{87}Sr/^{86}Sr$ ratios of 0.707073 to 0.707560 (Tian and Zeng, 1995; Qu et al., 2018). In addition, the reported $(^{87}Sr/^{86}Sr)_i$ of the ELIP basalts (out zone) lower than 0.7069 (0.704800 to 0.706900; Fan et al., 2008; Lai et al., 2012). In this study, the foot wallrock (siliceous limestone) and Mn ore samples have $^{87}Sr/^{86}Sr$ ratios (0.706897–0.707093, mean 0.706971) significantly lower than that of the upper Earth crust (up to 0.711900) (Palmer and Elderfield, 1985), and slightly lower than that of the Late Permian (end-Guadalupian) seawater (minimum 0.707073) (Tian and Zeng, 1995; Qu

Table 4
REE compositions (ppm) of hydrothermal and hydrogenous type Mn deposits from different localities. Table also include the Changgou Mn deposit.

Lacality	La	Ce	Pr	Nd	Sm	Eu	Gd	Tb	Dy	Ho	Er	Tm	Yb	Lu	ΣREE	Deposit type	References
Indian Ocean	153.40	714.10	34.80	142.00	33.80	8.90	43.70	5.70	30.60	5.60	15.50	2.30	15.00	2.20	1207.60	Hydrogenous	Nath et al. (1992)
Johnston Island	260.00	1201.00	44.80	192.70	35.40	10.10	48.50	6.80	43.70	9.90	28.90	4.30	27.90	3.90	1917.70	Hydrogenous	Wiltshire et al. (1999)
Pitcairn Island hotspot	276.80	741.70	50.80	214.40	42.70	10.20	49.90	7.20	44.70	9.20	26.40	3.90	26.00	4.00	1508.10	Hydrogenous	Glasby et al. (1997)
Indian Ocean	183.20	163.80	–	164.40	35.30	9.10	37.20	–	34.70	–	–	–	17.60	2.60	647.90	Hydrothermal	Nath et al. (1997)
East Pasific Rise	182.00	93.70	–	159.00	28.30	6.20	–	5.40	–	–	–	–	18.30	3.20	495.40	Hydrothermal	Piper and Graef (1974)
Neptuno deposit	125.20	289.30	24.40	78.40	12.80	7.20	10.30	1.30	6.60	1.10	3.10	0.30	2.30	0.30	563.10	Hydrothermal	Del Río Salas (2008)
Guichi deposit	58.40	60.90	12.50	49.80	11.30	2.61	11.70	1.70	9.49	2.05	5.33	0.71	3.89	0.60	231.00	Hydrothermal	Xie et al. (2013)
Germili deposit	192.10	79.80	47.80	195.90	35.50	8.60	37.90	6.40	32.50	5.80	17.20	2.10	14.10	1.90	677.60	Hydrothermal	Sasmaz et al., 2014
Zunyi deposit	116.00	91.00	14.00	57.20	9.38	2.24	12.50	1.80	11.60	2.71	7.36	0.92	5.26	0.80	332.77	This study	
Zunyi deposit	254.00	264.00	54.50	209.00	39.80	7.28	34.70	5.96	36.10	7.24	20.00	2.88	18.70	2.62	956.78		
Zunyi deposit	240.00	229.00	60.90	231.00	43.60	7.25	33.40	5.44	31.80	6.33	17.70	2.63	17.30	2.42	928.77		
Zunyi deposit	218.00	176.00	61.20	252.00	51.30	8.79	43.50	7.07	40.30	7.58	19.70	2.71	17.10	2.36	907.61		
Zunyi deposit	39.80	68.50	8.44	31.50	7.17	1.81	7.62	1.52	10.20	2.02	5.23	0.73	4.63	0.64	189.81		
Zunyi deposit	132.00	118.00	33.20	119.00	24.10	4.34	19.50	3.36	20.30	4.01	10.80	1.51	9.72	1.36	501.20		

et al., 2018), but close or slightly higher than that of the ELIP basalts (out zone) (0.704800–0.706900) (Fan et al., 2008; Lai et al., 2012; Bagherpour et al., 2018) (Fig. 11). This is likely caused by the mixing of deep-sourced Mn-rich hydrothermal fluid with seawater, resulting in the intermediate $^{87}Sr/^{86}Sr$ ratios for the Changgou samples. Hence, the Sr isotope features indicate that the primary input of Mn-rich hydrothermal fluids during the formation of the Changgou Mn deposit. The increasing $^{87}Sr/^{86}Sr$ trend from the foot wallrock (siliceous limestone) to the Mn orebody reflects weakening of hydrothermal flux and strengthening of seawater contribution in the late hydrothermal stage (Fig. 11).

5.2. Redox evolution of Changgou Mn deposit

Certain redox-sensitive trace elements (e.g., Mo, V, and U) are widely using as paleo-redox proxies due to their enrichments in reducing pelagic environment (Algeo and Tribovillard, 2009 and references therein). Previous studies suggested that the euxinic conditions can be assessed by the concentration of Mo in ancient fine-grained sedimentary rocks: >100 ppm Mo reflects bottom water with a permanently euxinic condition, whereas 25 to 100 ppm Mo reflects bottom water with an intermittently euxinic condition (Lyons et al., 2003; Scott and Lyons, 2012; Liao et al., 2019). The bulk Mo concentrations (31.00–138 ppm) of the lower wallrock (tuffaceous claystone) samples suggest intermittently euxinic conditions (Fig. 12). In addition, the sample CG-7 (tuffaceous claystone) has markedly higher Mo content (138 ppm) than the Mo threshold, which suggesting the transient euxinic condition present in the pre-mineralization.

Most study samples have decrease Mo/Al, V/Al, U/Al ratios from the footwalls to the orebody, and transition to the hanging-wall, indicating decreasing authigenic enrichment (Fig. 12; Tribovillard et al., 2006; Wei et al., 2019). In particular, most footwall samples have distinctly higher Mo/Al, V/Al, U/Al ratios, indicating moderately-strongly reducing conditions (Wei et al., 2019). Whereas these ratios decrease from orebody to the hanging-wall, which reflecting the euxinic transition to suboxic conditions (Fig. 12; Qiu et al., 2014).

In general, Mo and U have similar geochemical behavior due to Mo and U exist as conservative oxyanions in the seawater (Liao et al., 2019). Notably, Mo in sediments tends to be enriched in the euxinic conditions, whereas U tends to be enriched in the suboxic conditions (Tribovillard et al., 2012; Liao et al., 2019). Accordingly, Algeo and Tribollivard (2009) proposed the discrimination diagram for this differential partitioning using the Mo_{EF} vs. U_{EF} scatter-plot (X_{auth}: the authigenic fraction of element X). In our case, almost all samples from the footwall show strongly Mo_{auth} (mean Mo_{EF} = 81.8) and U_{auth} (mean U_{EF} = 33.2) enrichments relative to Average Upper Continental Crust (AUCC), indicating anoxic-euxinic conditions (Fig. 13). Of particular importance is sample CG-6 show moderately Mo_{auth} (Mo_{EF} = 14.1) and U_{auth} (U_{EF} = 9.4) enrichment, whereas the two samples adjacent to sample CG-6 show strongly Mo_{auth} and U_{auth} enrichments (CG-5: Mo_{EF} = 80.2, U_{EF} = 50.5; CG-7: Mo_{EF} = 125.9, U_{EF} = 12.8), suggesting that a transient suboxic event was present in the footwall. The majority of ore samples display moderately Mo_{auth} and U_{auth} enrichments (mean Mo_{EF} = 13.4, U_{EF} = 5.5) (Fig. 13), indicating suboxic-anoxic conditions during the mineralization. However, data from the hanging-wall are mostly indicative of suboxic (and frequently suboxic-oxic) due to the weak Mo_{auth} and moderate U_{auth} enrichments (mean Mo_{EF} = 1.5, U_{EF} = 8.9). Accordingly, the bottom-water was likely euxinic-anoxic (sporadically suboxic) transition to primarily anoxic-suboxic (from the footwall to the orebody) and then transition to oxic in the hanging-wall (Fig. 13).

The geochemical behavior of Ce in seawater is significantly different from that of other REEs, which is important for sedimentary environment reconstruction (Wright and Holser, 1987; Holser, 1997; Pattan et al., 2005). The Ce_{anom} ($=\lg[3Ce_{SN}/(2 \times La_{SN} + Nd_{SN})]$, where SN = shale normalized to PAAS (McLennan, 1989)) can indicate the redox conditions of ancient seawater, i.e., $Ce_{anom} > -0.1$ and < -0.1 indicates oxidizing and reducing water body, respectively (Wright and

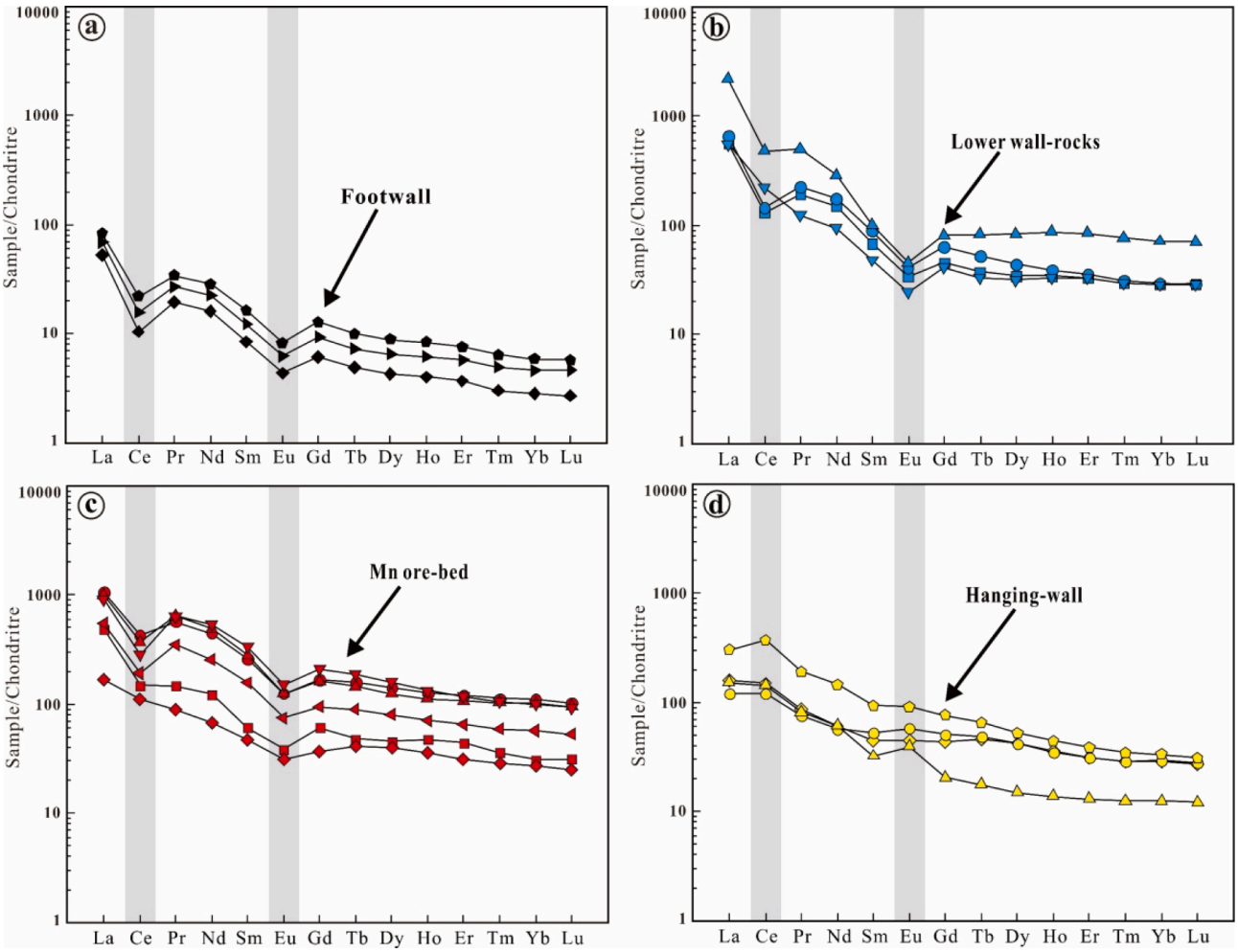

Fig. 10. Chondrite-normalized REE patterns for the various wallrocks and Mn ores from the Changgou. Chondrite data are from Sun and McDonough (1989). (a) footwall; (b) The lower wallrock; (c) Mn ores; (d) Hanging-wall.

Holser, 1987). In our cases, the low Ce_{anom} (mean − 0.45) of all the footwall samples indicate anoxic conditions were presented in the pre-mineralization. Furthermore, all the ore samples have slightly higher Ce_{anom} (mean − 0.31, still below − 0.1), except for the sample CG-13 (−0.07), which implies more anoxic-suboxic conditions during the mineralization process. The hanging-wall samples have Ce_{anom} (mean 0.1) high than − 0.1, indicating oxic conditions in the post-mineralization. Consequently, the Ce_{anom} also support that the redox condition evolved from anoxic to anoxic-suboxic from the footwall deposition to mineralization, and then to oxic in the hanging-wall deposition.

5.3. *Implications for Mn metallogenic mechanism*

The Central Guizhou basin was formed by the varying crustal subsidence caused by the ELIP updoming, and accompanied by a series of volcanism/hydrothermal activities (Liu et al., 1989; Chen et al., 2003; He et al., 2006). Meanwhile, continuous regional extension may have further enlarged the rift basin and generated the associated *syn*-sedimentary tectonics (Liu et al., 1989, 2008, 2019) that later served as channels for the Mn-rich hydrothermal fluid migration.

Typical sedimentary exhalative structures, including detrital and brecciated ones observed in Changgou Mn ore samples, point to the impact of hydrothermal activity during the Mn mineralization. Meanwhile, the crosscutting of rhodochrosite by capillitite and manganoan calcite veins (Fig. 6) does not resemble ore textures formed by normal marine sedimentation. The more reasonable explanation is these textures were the result of crosscutting or filling of Mn-rich hydrothermal fluids in the later stage. This result indicates that Mn-rich hydrothermal fluids were causative to the Mn mineralization. Numerous hydrothermal minerals (e.g. galena, sphalerite, siegenite, molybdenite, barite, rutile, and monazite) (Fig. 7) were detected in the ore samples, which also supported a hydrothermal origin for the Mn mineralization. Recently, Yan et al. (2020) analyzed the footwall and hanging-wall claystone of the Nancha Mn deposit (Zunyi orefield) and suggested that they were sourced from the ELIP mafic tuff, reflecting a genetic link between Mn mineralization and ELIP volcanism. In addition, zircon ages from the footwall and hanging-wall claystone (Nancha Mn deposit, Zunyi orefield) (262.5–261.6 Ma; Yan et al., 2020) are older than the ELIP subaerial eruptive phase (260.4–259.1 Ma; Zhong et al., 2014; Huang et al., 2016), but are comparable to the eruption of early-stage ELIP submarine pillow basalts or mafic volcaniclastic debris (~263 Ma; Sun et al., 2010). This indicates that the Zunyi Mn deposit in the Central Guizhou basin was formed during the early-stage ELIP subaqueous mafic volcanism. Accordingly, integrating the above discussion, the Mn mineralization has most probably resulted from hydrothermal events related to early-stage ELIP subaqueous volcanism.

The significant redox changes (anoxic to suboxic/oxic) may have also played a critical role for the Mn ore formation in the Zunyi orefield. The Central Guizhou basin was a restricted basin and was interpreted as the depositional center (surrounded by carbonate platform) during the end-Guadalupian (Wei et al., 2016). Moreover, the end-Guadalupian

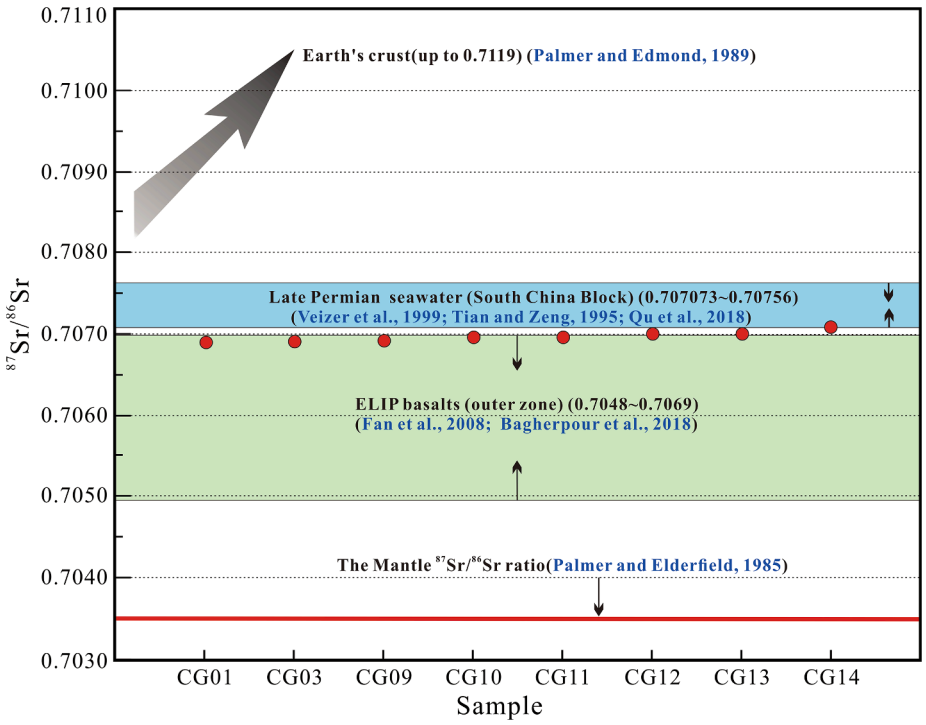

Fig. 11. Sr isotope compositions of the Changgou Mn deposit. $^{87}Sr/^{86}Sr$ data source: Continent (Palmer and Elderfield, 1985); Late Permian Maokou-stage seawater in the South China Block (Veizer et al., 1999; Tian and Zeng, 1995; Qu et al., 2018); $(^{87}Sr/^{86}Sr)_i$ ELIP basalts (out zone) (Fan et al., 2008; Bagherpour et al., 2018); Mantle (Palmer and Edmond, 1989).

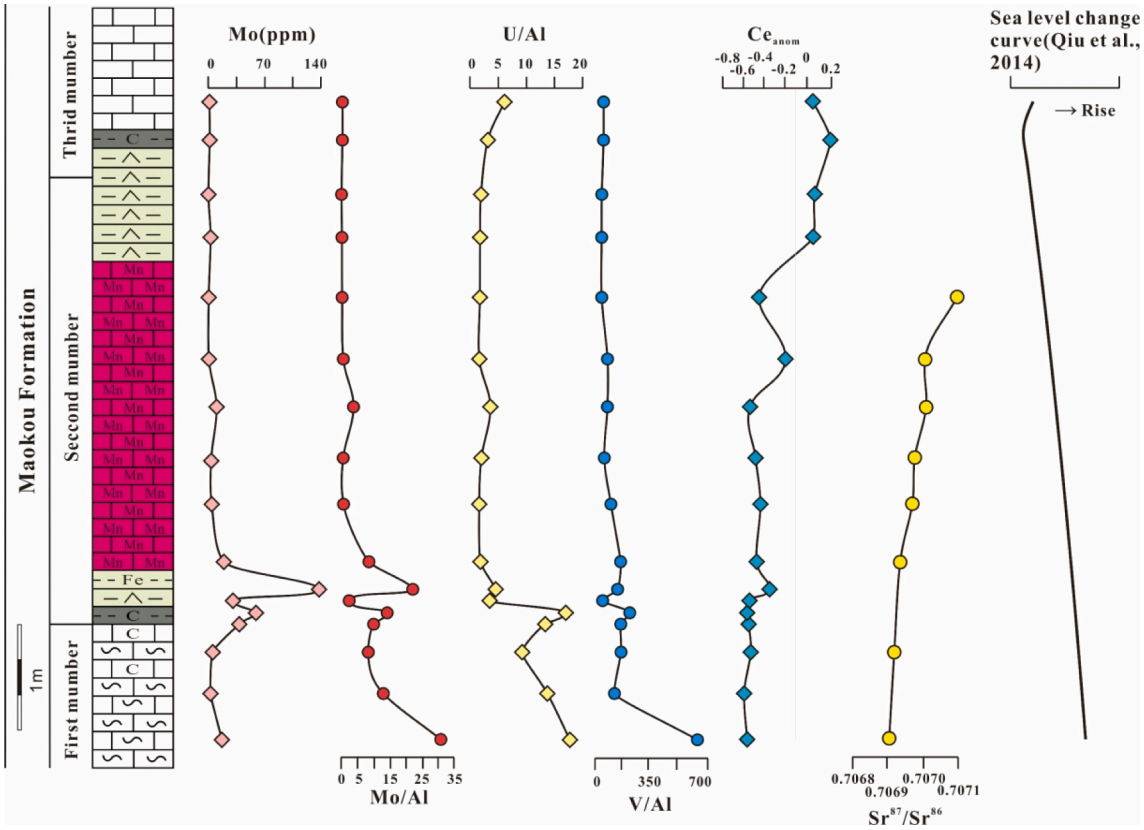

Fig. 12. Lithological and geochemical stratigraphy for the Changgou Mn deposit, displaying changes in Mo/Al, U/Al, V/Al, Ce_{anom}, and $^{87}Sr/^{86}Sr$. Date source: Sea level change (Qiu et al., 2014).

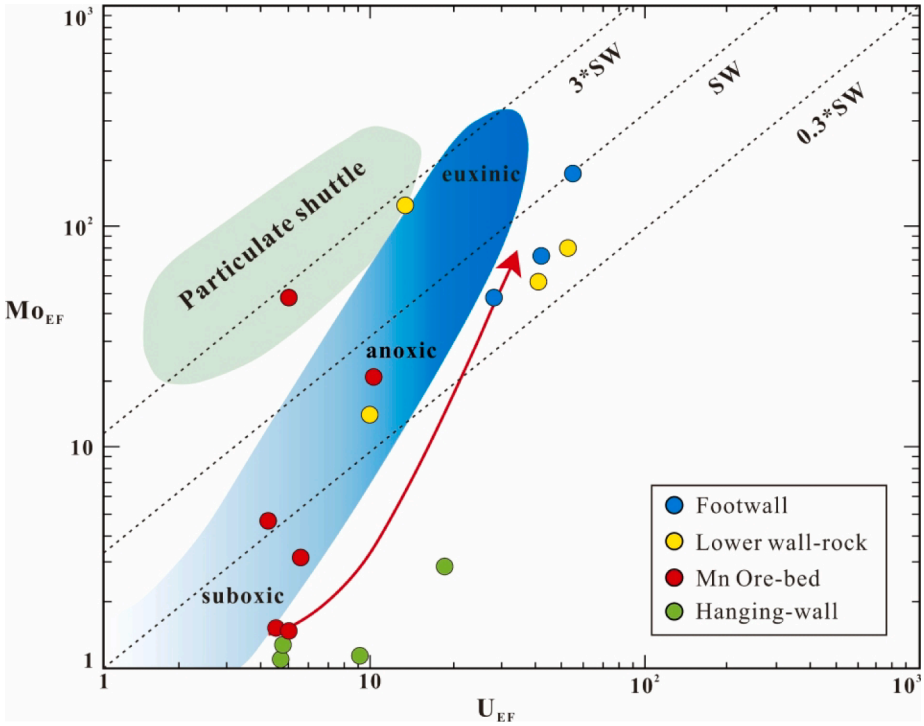

Fig. 13. Plot of Mo_{EF} versus U_{EF} of the Changgou Mn deposit. The distinguishing criteria area after Algeo and Tribollivard (2009). Abbreviations: EFs = enrichment factors; X_{EF} = [(X/Al) $_{sample}$/(X/Al) $_{AUCC}$]; X = wt.% of selected elements; AUCC = Average Upper Continental Crust (McLennan, 2001).

large-scale regression resulted in the slowed water-mass circulation in the restricted basin (Haq and Schutter, 2008). Meanwhile, ocean acidification (Payne et al., 2010; Beauchamp and Grasby, 2012) and global warming (Davydov et al., 2016) caused by coeval volcanism further limited water-mass circulation. In addition, the lower oxygen content of the coeval atmosphere (Glasspool and Scott, 2010), and the seawater oxygen supply may have reduced due to the eustatic sea-level drop (which decreased water circulation in deep basins) (Wei et al., 2016, 2019). These events likely induced frequent euxinic/anoxia events in the deep-water of the restricted Central Guizhou basin. Under such circumstances, Mn-rich hydrothermal fluids were likely released through the syn-sedimentary faults, and the manganese occurred as Mn^{2+} in the anoxic deep-water zones in the basin. However, the large-scale regression has also triggered frequent water-body shoaling and caused downward migration of the redox interface in the restricted basin (Zhang et al., 2015; Wei et al., 2016, 2019), which would enhance the dissolved oxygen dissolution and concentrations in the anoxic deep-water zones. Under these circumstances, the dissolved Mn^{2+} was oxidized as Mn-oxyhydroxide in the overlying oxic-suboxic water zones and precipitated (Wu et al., 2016). During the sediment diagenesis, the buried Mn-oxyhydroxide was reduced to Mn^{2+} and combined with bicarbonate released by sediments (Wu et al., 2016), and forming the manganese carbonates observed.

Integrating the above discussion, the ELIP volcanism likely provided a favorable source-migration-sink system for the Mn mineralization. The hydrothermal activity caused by the early-stage ELIP subaqueous volcanism supplied much of the ore-forming materials, and the Central Guizhou rift basin with syn-sedimentary structures (formed by the differential subsidence) likely provided efficient ore-fluid migration channels and precipitation site for Mn mineralization. Meanwhile, the significant redox changes have caused the Mn precipitation in the Central Guizhou basin.

6. Conclusions

Mineralogical features, whole-rock geochemistry, and Sr isotope data from the Permian Changgou Mn deposit (western South China Block) reveal that the ore-forming fluids were primarily originated from hydrothermal events related to the early-stage ELIP subaqueous volcanism. Redox proxies imply that the redox conditions of the sedimentary system changed from euxinic-anoxic (footwall deposition), through anoxic-suboxic (Mn mineralization) to oxic (hanging-wall deposition). Such redox changes were probably resulted from a combination of the rapid sea-level regression and enhanced seawater dissolved oxygen supply. Manganese was likely initially enriched as Mn^{2+} in the anoxic deep-water zones of the Central Guizhou basin, and subsequently oxidized to Mn oxyhydroxide in the overlying suboxic waters and precipitated into the sediments, and then transformed into Mn carbonate during sediment diagenesis. Consequently, the ELIP-related tectonic-hydrothermal activities and significant redox changes have provided a favorable source-migration-sink system for the Mn mineralization in the Central Guizhou basin.

Declaration of Competing Interest

The authors declare that they have no known competing financial interests or personal relationships that could have appeared to influence the work reported in this paper.

Acknowledgments

This research was funded by the Scientific and Technological Innovation Team of Sedimentary Deposits in Guizhou Province (2018-5613), the National Natural Science Foundation of China (U1812402), and the Talent Base in Guizhou Province (RCJD2018-21). Comments from the editor and two anonymous reviewers have significantly enhanced the manuscript.

Appendix A. Supplementary data

Supplementary data to this article can be found online at https://doi.org/10.1016/j.oregeorev.2021.103993.

References

Albuquerque, M.F.S., Horbe, A.M.C., Botelho, N.F., 2017. Genesis of Mn deposits in southwestern Amazonia: Mineralogy, geochemistry and paleoenvironment. Ore Geol. Rev. 89, 270–289.

Algeo, T.J., Tribovillard, N., 2009. Environmental analysis of paleoceanographic systems based on molybdenum–uranium covariation. Chem. Geol. 268, 211–225.

Ali, J.R., Thompson, G.M., Zhou, M.F., Song, X.Y., 2005. Emeishan Large Igneous Province, SW China. Lithos 79, 475–489.

Bagherpour, B., Bucher, H., Hermann, E.S., Vennemann, T., Chiaradia., M., Shen, S.Z.,, 2018. Early Late Permian coupled carbon and strontium isotope chemostratigraphy from South China: Extended Emeishan volcanism? Gondwana Res. 58, 58–70.

Bau, M., Dulski, P., 1999. Comparing yttrium and rare earths in hydrothermal fluids from the Mid-Atlantic Ridge: implications for Y and REE behavior during near-vent mixing and for the Y/Ho ratio of Proterozoic seawater. Chem. Geol. 155 (1–2), 77–90.

Beauchamp, B., Grasby, S.E., 2012. Permian lysocline shoaling and ocean acidification along NW Pangea led to carbonate eradication and chert expansion. Palaeogeogr. Palaeoclimatol. Palaeoecol. 350, 73–90.

Bonatti, E., Kraemer, T., Rydel, H., 1972. Classification and genesis of submarine iron–manganese deposits. In: Horn, D.R. (Ed.), Ferromanganese Deposits on the Ocean Floor. Natl Sci. Found, Washington, DC, pp. 149–166.

Chen, F., Xue, W., Yan, J., Wignall, P.B., Meng, Q., Luo, J., Feng, Q., 2018a. Alatoconchids: giant Permian bivalves from South China. Earth Sci. Rev. 179, 147–167.

Chen, S., Yin, X.B., Wang, X.Y., Huang, X., Ma, Y., Guo, K., Zeng, Z.G., 2018b. The geochemistry and formation of ferromanganese oxides on the eastern flank of the Gagua ridge. Ore Geol. Rev. 95, 118–130.

Chen, W.Y., Liu, J.R., Wang, Z.G., Zheng, Q.L., 2003. During the Permian Emeishan basalt explosion in Guizhou Province. J. Palaeogeogr. 5 (1), 17–28 (in Chinese with English abstract).

Choi, J.H., Hariya, Y., 1992. Geochemistry and depositional environment of Mn oxide deposits in the Tokora Belt, northeastern Hokkaido. Japan. Econ. Geol. 87, 1265–1274.

Condie, K.C., 1993. Chemical composition and evolution of the Upper Continental Crust: contrasing results from surface samples and shales. Chem. Geol. 104, 1–37.

Davydov, V.I., Biakov, A.S., Isbell, J.L., Crowley, J.L., Schmitz, M.D., Vedernikov, I.L., 2016. Middle Permian U-Pb zircon ages of the “glacial” deposits of the Atkan Formation, Ayan-Yuryakh anticlinorium, Magadan province, NE Russia: Their significance for global climatic interpretations. Gondwana Res. 38, 74–85.

Del RioSalas, R., Ruiz, J., Ochoa-Landín, L., Noriega, O., Barra, F., Meza-Figueroa, D., Paz-Moreno, F., 2008. Geology, Geochemistry and Re–Os systematics of manganese deposits from the Santa Rosalía Basin and adjacent areas in Baja California Sur, México. Miner. Deposita 43 (4), 467–482.

Fan, D.L., Yang, P.J., 1999. Introduction to and classification of manganese deposits of China. Ore Geol. Rev. 15, 1–13.

Fan, W.M., Zhang, C.H., Wang, Y.J., Guo, F., Peng, T., 2008. Geochronology and geochemistry of Permian basalts in western Guangxi Province, Southwest China: evidence for plume-lithosphere interaction. Lithos 102, 218–236.

Fu, Y., Xu, Z.G., Pei, H.X., Jiang, R., 2014. Study on metallogenic regularity of manganese ore deposits in China. Acta Petrol. Sin. 88, 2192–2207 (in Chinese with English abstract).

Gao, J.B., Yang, R.D., Xu, H., Zhang, X., Chen, J., Zheng, L.L., 2018. Genesis of Permian sedimentary Mn deposits in Zunyi, Guizhou Province, SW China: Constraints from geology and elemental geochemistry. J. Geochem. Explor. 192, 142–154.

Glasby, G.P., Stüben, D., Jeschke, G., Stoffers, P., Garbe-Schönberg, C.D., 1997. A model for the formation of hydrothermal manganese crusts from the Pitcairn Island hotspot. Geochim. Cosmochim. Acta 61, 4583–4597.

Glasspool, I.J., Scott, A.C., 2010. Phanerozoic concentrations of atmospheric oxygen reconstructed from sedimentary charcoal. Nat. Geosci. 3, 627–630.

Haq, B.U., Schutter, S.R., 2008. A chronology of Paleozoic sea-level changes. Science 322, 64–68.

Hayashi, K.I., Fujisawa, H., Holland, H.D., Ohmoto, H., 1997. Geochemistry of 1.9 Ga sedimentary rocks from Northeastern Labrador. Canada. Geochim. Cosmochim. Acta 61, 4115–4137.

He, B., Xu, Y., Wang, Y., Luo, Z., 2006. Sedimentation and lithofacies paleogeography in southwestern China before and after the Emeishan flood volcanism: New insights into surface response to mantle plume activity. J. Geol. 114, 117–132.

Hein, J.R., Kosk, R.A., 1987. Bacterially mediated diagenetic origin for chert-hosted manganese deposits in the Franciscan Complex. Calif. Coast Range. Geol. 15 (8), 722–726.

Hein, J.R., Schulz, M.S., Kang, J.K., 1990. Insular and submarine ferromanganese mineralization of the Tonga-Lau region. Mar. Min. 9, 305–354.

Hein, J.R., Schulz, M.S., Dunham, R.E., Stern, R.J., Bloomer, S.H., 2008. Diffuse flow hydrothermal manganese mineralization along the active Mariana and southern Izu-Bonin arc system, western Pacific. J. Geophys. Res. 113, 1–29.

Huang, H., Cawood, P.A., Hou, M.C., Yang, J.H., Ni, S.J., Du, Y.S., Yan, Z.K., Wang, J., 2016. Silicic ash beds bracket Emeishan large igneous province to b1 m.y. at ~260 Ma. Lithos 264, 17–27.

Holser, W.T., 1997. Evaluation of the application of rare-earth elements to paleoceanography. Palaeogeogr. Palaeoclimatol. Palaeoecol. 132, 309–323.

Hou, Z.L., Xue, Y.Z., Huang, J.S., Zhu, K.J., Lin, Y.H., Liu, H.J., Yao, J.Q., Zhu, K.J., 1997. Manganese Ore Deposits Around Yangtze Block. Metallurgical Industry Press, Beijing, 350p (in Chinese).

Josso, P., Pelleter, E., Pourret, O., Fouquet, Y., Etoubleau, J., Cheron, S., Bollinger, C., 2017. A new discrimination scheme for oceanic ferromanganese deposits using high field strength and rare earth elements. Ore Geol. Rev. 87, 3–15.

Korte, C., Kozur, H.W., Bruckschen, P., Veizer, J., 2003. Strontium isotope evolution of Late Permian and Triassic Seawater. Geochim. Cosmochim. Acta 67 (1), 47–62.

Lai, S.C., Qin, J.F., Li, Y.F., Li, S., Santosh, M., 2012. Permian high Ti/Y basalts from the eastern part of the Emeishan Large Igneous Province, southwestern China: petrogenesis and tectonic implications. J. Asian Earth Sci. 47, 216–230.

Liakopoulos, A., Glasby, G.P., Papavassiliou, C.T., Boulegue, J., 2001. Nature and origin of the Vani Mn deposit, Misos, Greece: an overview. Ore Geol. Rev. 18, 181–209. https://doi.org/10.1016/S0169-1368(01)00029-4.

Liao, Z.W., Hu, W.X., Cao, J., Wang, X.L., Fu, X.G. 2019. Oceanic anoxia through the late Permian Changhsingian Stage in the Lower Yangtze region, South China: Evidence from sulfur isotopes and trace elements. Chem. Geol. https://doi.org/10.1016/j.chemgeo.2019.119371.

Li, C.F., Wang, X.C., Guo, J.H., Chu, Z.Y., Feng, L.J., 2016. Rapid separation scheme of Sr, Nd, Pb and Hf from a single rock digest using a tandem chromatography column prior to isotope ratio measurements by mass spectrometry. J. Anal. At. Spectrom. 31, 1150–1159.

Liu, X.F., Wang, Q.S., Gao, X.J., 1989. Mn deposits of Guizhou, China: Guiyang: Guizhou people’s Press, pp. 7-56. (in Chinese).

Liu, P., Liao, Y.C., Yin, K.H., Ye, D.S., Zhu, H., Han, Z.H., Yang, G.L., 2008. Hydrothermal sedimentary Mn deposits associated to volcanic activities-Permian Mn deposit in Guizhou. Geol. China 35 (5), 992–1006 (in Chinese with English abstract).

Liu, Z.C., Wang, C., Zhang, Y.G., Fang, B., Chen, D., 2015. Geochemistry and ore genesis of Zunyi Mn deposit, Guizhou Province. China. Acta Mineralogica Sinica 35 (4), 481–488 (in Chinese with English abstract).

Liu, Z.C., Zhou, Q., Yan, J.X., Wang, Y., Chen, D., Zhong, Y.L., Qin, X.J., 2019. Structure of Zunyi rift basin in Guizhou Province during the Permian and its controlling on manganese deposits. J. Palaeogeogr. Chinese Ed. 21 (3), 517–526 (in Chinese with English abstract).

Lyons, T.W., Werne, J.P., Hollander, D.J., Murray, R.W., 2003. Contrasting sulfur geochemistry and Fe/Al and Mo/Al ratios across the last oxic–to–anoxic transition in the Cariaco Basin, Venezuela. Chem. Geol. 195, 131–157.

Maghfouri, S., Rastad, E., Mousivand, F., Choulet, F., Ye, L., 2017. Geological and geochemical constraints on the Cheshmeh-Frezi volcanogenic stratiform Mn deposit, southwest Sabzevar basin, Iran. Ore Geol. Rev. 89, 96–113.

McLennan, S.M., 1989. Rare earth elements in sedimentary rocks; influence of provenance and sedimentary processes. Rev. Mineral. Geochem. 21, 169–200.

McLennan, S.M., 2001. Relationships between the trace element composition of sedimentary rocks and upper continental crust. Geochem. Geophys. Geosyst. 2 (4), 1–24.

Mills, R.A., Wells, D., Roberts, S., 2001. Genesis of ferromanganese crusts from the TAG hydrothermal field. Chem. Geol. 176, 3–293.

Nath, B.N., Balaram, V., Sudhakar, M., Plüger, W.L., 1992. Rare earth element geochemistry of ferromanganese deposits of the Indian Ocean. Mar. Chem. 38, 185–208.

Nath, B.N., Plüger, W.L., Roelandts, I. 1997. Geochemical constraints on the hydrothermal origin of ferromanganese encrustations from the Rodriguez Triple Junction, Indian Ocean. In: Nicholson, K., Hein, J.R., Bühn, B., Dasgupta, S. (Eds.), Manganese mineralization: Geochemistry and mineralogy of terrestrial and marine deposits. Geol. Soc. Spl. Pub., 119, pp. 199–211.

Nicholson, K., 1992. Contrasting mineralogical–geochemical signatures of manganese oxides: Guides to metallogenesis. Econ. Geol. 87, 1253–1264.

Nicholson, K., Nayak, V.K., Nanda, J.K., 1997. Mn ores of the Ghoriajhor-Monmunda area, Sundergarh District, Orissa, India: Geochemical evidence for a mixed Mn source. Geol. Soc. Lond. Spec. Pub. 119, 117–121.

Nozaki, Y., Zhang, J., Amakawa, H., 1997. The fractionation between Y and Ho in the marine environment. Earth Planet. Sci. Lett. 148, 329–340.

Nyame, F.K., Beukes, N.J., Kase, K., Yamamoto, M., 2002. Compositional variations in manganese carbonate micronodules from the Lower Proterozoic Nsuta deposit, Ghana: product of authigenic precipitation or post-formational diagenesis. Sediment. Geol. 154 (3–4), 159–175.

Palmer, M.R., Edmond, J.M., 1989. The strontium isotope budget of the modern ocean. Earth Planet. Sci. Lett. 92 (92), 11–26. https://doi.org/10.1016/0012-821X(89)90017-4.

Palmer, M.R., Elderfield, H., 1985. Sr isotope composition of sea water over the past 75 Myr. Nature 314 (314), 526–528.

Pattan, J.N., Pearce, N.J.G., Mislankar, P.G., 2005. Constraints in using cerium-anomaly of bulk sediments as an indicator of paleo bottom water redox environment: a case study from the Central Indian Ocean Basin. Chem. Geol. 2005 (221), 260–278.

Payne, J.L., Turchyn, A.V., Paytan, A., DePaolo, D.J., Lehrmann, D.J., Yu, M.Y., Wei, J.Y., 2010. Calciumisotope constraints on the end–Permianmass extinction. Proc. Natl. Acad. Sci. U.S.A. 107, 8543–8548.

Papavassiliou, V.K., Glasby, G., Alfieris, D., Mitsis, I., 2017. New geochemical and mineralogical constraints on the genesis of the Vani hydrothermal Mn deposit at NW Milos island, Greece: Comparison with the Aspro Gialoudi deposit and implications for the formation of the Milos Mn mineralization. Ore Geol. Rev. 80, 594–611.

Piper, D.Z., Graef, P.A., 1974. Gold and rare earth elements in sediments from the East Pacific rise. Mar. Geol. 17, 287–297.

Qiu, Z., Wang, Q., Zou, C., Yan, D., Wei, H., 2014. Transgressive-regressive sequences on the slope of an isolated carbonate platform (Middle-Late Permian, Laibin, South China). Facies 60, 327–345.
Qu, H.J., Wang, L., Guan, L.Q., Fan, Y.Q., Luo, T.W., 2018. Strontium isotopic evolution characteristics and its geological significance of Permian in the northern upper Yangtze region. Earth Sci. 1–20 (in Chinese with English abstract).
Rodríguez-Díaz, A.A., Canet, C., Villanueva-Estrada, R.E., Chacón, E., Gervilla, F., Velasco-Tapia, F., Cruz-Gámez, E.M., Eduardo González-Partida, E.G., Casas-García, R., Carlos Linares-López, C., Daniel Pérez-Zárate, D., 2018. Recent Mn-Ag deposits in coastal hydrothermal springs in the Baja California Peninsula, Mexico. Miner. Deposita 1–18.
Sabatino, N., Neri, R., Bellanca, A., Jenkyns, H.C., Masetti, D., Scopelliti, G., 2011. Petrography and high-resolution geochemical records of Lower Jurassic Mn-rich deposits from Monte Mangart, Julian Alps. Palaeogeogr. Palaeoclimatol. Palaeoecol. 299, 97–109.
Sasmaz, A., Turkyilmaz, B., Ozturk, N., Yavuz, F., Kumral, M., 2014. Geology and geochemistry of Middle Eocene Maden complex ferro-Mn deposits from the Elazığ-Malatya region, eastern Turkey. Ore Geol. Rev. 56, 352–372.
Scott, C., Lyons, T.W., 2012. Contrasting molybdenum cycling and isotopic properties in euxinic versus non–euxinic sediments and sedimentary rocks: refining the paleoproxies. Chem. Geol. 324, 19–27.
Shellnutt, J.G., 2014. The Emeishan large igneous province: A synthesis. Geosci. Front. 5, 369–394.
Sugitani, K., Horiuchi, Y., Adachi, M., Sugisaki, R., 1996. Anomalously low Al_2O_3/TiO_2 ratios for Archean cherts from the Pilbara Block, Western Australia–possible evidence for extensive chemical weathering on the early earth. Precambrian Res. 80, 49–76.
Sun, S.S., Mcdonough, W.F., 1989. Chemical and isotopic systematics of oceanic basalts: implications for mantle composition and processes. Geological Society London Special Publications 42, 313–345.
Sun, Y.D., Lai, X.L., Wignall, P.B., Widdowson, M., Ali, J.R., Jiang, H.S., Wang, W., Yan, C.B., Bond, D.P., Védrine, S., 2010. Dating the onset and nature of the middle Permian Emeishan large igneous province eruptions in SW China using conodont biostratigraphy and its bearing on mantle plume uplift models. Lithos 119, 20–33.
Taylor, S.R., McLennan, S.M., 1985. In: The Continental Crust: Its Composition and Evolution. Blackwell Scientific Publications, Oxford, pp. 1–312.
Tian, J.C., Zeng, Y.F., 1995. The revolution of the isotopic composition of Strontium in the Permian Paleo-Ocean in south China. Acta Sedimentol. Sinica 13, 125–130 (in Chinese with English abstract).
Toth, J.R., 1980. Deposition of submarine crusts rich in Mn and iron. Geol. Soc. Am. Bull. 91, 44–54.
Tribovillard, N., Algeo, T.J., Lyons, T., Riboulleau, A., 2006. Trace metals as paleoredox and paleoproductivity proxies: an update. Chem. Geol. 232, 12–32.
Tribovillard, N., Algeo, T.J., Baudin, F., Riboulleau, A., 2012. Analysis of marine environmental conditions based on molybdenum–uranium covariation—Applications to Mesozoic paleoceanography. Chem. Geol. 324, 46–58.
Ukstins-Peate, I., Bryan, S.E., 2008. Re-evaluating plume-induced uplift in the Emeishan Large Igneous Province. Nat. Geosci. 1 (9), 625–629.
Veizer, J., Compston, W., 1974. 87Sr/86Sr composition of seawater during the Phanerozoic. Geochim. Cosmochim. Acta 38, 1461–1484.
Veizer, J., Ala, D., Azmy, K., Bruckschen, P., Buhl, D., Bruhn, F., Carden, G.A.F., Diener, A., Ebneth, S., Goddéris, Y., Jasper, T., Korte, C., Pawellek, F., Podlaha, O.G., Strauss, H., 1999. 87Sr/86Sr, $\delta^{13}C$ and $\delta^{18}O$ evolution of Phanerozoic seawater. Chem. Geol. 161, 59–88.
Wang, Y., Liu, Z.C., Chen, D., Zhong, Y.L., Qin, X.J., 2018. Discovery of submarine gas-liquid spout group and its significance in Permian manganese deposit in Zhunyi of Guizhou. Guizhou Geol. 35, 81–87 (in Chinese with English abstract).
Wei, H.Y., Wei, X.M., Qiu, Z., Song, H.Y., Shi, G., 2016. Redox conditions across the G-L boundary in South China: Evidence from pyrite morphology and sulfur isotopic compositions. Chem. Geol. 440, 1–14.
Wei, H.Y., Tang, Z.W., Yan, D.T., Jianguo Wang, J.G., Roberts, Andrew P., A.P.,, 2019. Guadalupian (Middle Permian) ocean redox evolution in South China and its implications for mass extinction. Chem. Geol. 530, 1–14.
Wu, C.Q., Zhang, Z.W., Xiao, J.F., Fu, Y.Z., Shao, S.X., Zheng, C.F., Yao, J.H., Xiao, C.Y., 2016. Nanhuan manganese deposits within restricted basins of the southeastern Yangtze Block, China: Constraints from geological and geochemical evidence. Ore Geol. Rev. 75, 76–99.
Wiltshire, J.C., Wen, X.Y., Yao, D., 1999. Ferromanganese crusts near Johnston Island: Geochemistry, stratigraphy and economic potential. Mar. Georesour. Geotechnol. 17, 257–270.
Wright, J., Holser, W.T., 1987. Paletedox variations in ancient oceans recorded by rare earth elements in fossil apatite. Geochim. Cosmochim. Acta 51, 631–644.
Xie, J.C., Sun, W.D., Du, J.G., Xu, W., Wu, L.B., Yang, X.Y., Zhou, T.F., 2013. Geochemical studies on Permian manganese deposits in Guichi, Eastern China: implications for their origin and formative environments. J. Asian Earth Sci. 74, 155–166.
Xu, H., Gao, J.B., Yang, R.D., Du, L.J., Liu, L.Z., Chen, J., Feng, K.L., Yang, G.H., 2020. Genesis for rare earth elements enrichment in the Permian manganese deposits in Zunyi, Guizhou Province, SW China. Acta Geol. Sinica English Ed. 94 (1), 90–102. https://doi.org/10.1111/1755-6724.14338.
Xu, Y.G., Wang, Y., Wei, G., He, B., 2013. Mantle plume-related mineralization and their principal controlling factors. Acta Petrol. Sinica 29 (10), 3307–3322 (in Chinese with English abstract).
Yang, R.D., Cheng, M.L., Gao, J.B., Xu, H., Li, J., Chen, J., Liu, K., 2018. The sedimentary characteristic and origin of Mn deposit in the middle Permian Maokou formation in Guizhou, China. Acta Geol. Sinica 92, 804–816 (in Chinese with English abstract).
Yan, H., Pi, D.H., Jiang, S.Y., Hao, W.D., Mänd, K., Robbins, L.J., Li, L., Konhauser, K.O., 2020. New constraints on the onset age of the Emeishan LIP volcanism and implications for the Guadalupian mass extinction. Lithos 360–361, 1–14.
Zhang, G., Zhang, X., Li, D., Farquhar, J., Shen, S., Chen, X., Shen, Y., 2015. Widespread shoaling of sulfidic waters linked to the end-Guadalupian (Permian) mass extinction. Geology 43, 1091–1094.
Zhou, M.F., Zhao, J.H., Qi, L., Su, W.C., Hu, R., 2006. Zircon U-Pb geochronology and elemental and Sr–Nd isotope geochemistry of Permian mafic rocks in the Funing area, SW China. Contrib. Mineral. Petr. 151, 1–19.
Zhou, Q., Du, Y.S., Qin, Y., 2013. Ancient natural gas seepage sedimentary-type manganese metallogenic system and ore-forming model: A case study of 'Datangpo type' manganese deposits formed in rift basin of Nanhua Period along Guizhou-Hunan-Chongqing border area. Mineral Deposits 32, 457–466 (in Chinese with English abstract).
Zhong, Y., Chen, Z., González, F.J., Hein, J.R., Zheng, X., Li, G., Luo, Y., Mo, A., Tian, Y., Wang, S., 2017. Composition and genesis of ferromanganese deposits from the northern South China Sea. J. Asian Earth Sci. 138, 110–128.
Zhong, Y., Liu, Q.S., Chen, Z., Gonzáleze, F.G., Hein, J.R., Zhang, J., Zhong, L.F., 2019. Tectonic and paleoceanographic conditions during the formation of ferromanganese nodules from the northern South China Sea based on the high-resolution geochemistry, mineralogy and isotopes. Mar. Geol. 410, 146–163.
Zhong, Y.T., He, B., Mundil, R., Xu, Y.G. 2014. CA-TIMS zircon U-Pb dating of felsic ignimbrite from the Binchuan section: implications for the termination age of Emeishan large igneous province. Lithos 204, 14–19.